Free-Surface Quasigeostrophy:
Bridging the gap between surface quasigeostrophy and the shallow-water equations

by

Ross Tulloch

B.A.Sc., Simon Fraser University, 2002

A THESIS SUBMITTED IN PARTIAL FULFILLMENT
OF THE REQUIREMENTS FOR THE DEGREE OF
MASTER OF SCIENCE
in the Department
of
Mathematics

SIMON FRASER UNIVERSITY
August 2003

PARTIAL COPYRIGHT LICENCE

I hereby grant to Simon Fraser University the right to lend my thesis, project or extended essay (the title of which is shown below) to users of the Simon Fraser University Library, and to make partial or single copies only for such users or in response to a request from the library of any other university, or other educational institution, on its own behalf or for one of its users. I further agree that permission for multiple copying of this work for scholarly purposes may be granted by me or the Dean of Graduate Studies. It is understood that copying or publication of this work for financial gain shall not be allowed without my written permission.

Title of Thesis/Project/Extended Essay:

Free-Surface Quasigeostrophy: Bridging the gap between surface quasigeostrophy and the shallow-water equations.

Author:

_____
(Signature)

Ross Tulloch
(Name)

August 8, 2003
(Date)

APPROVAL

Name:	Ross Tulloch
Degree:	Master of Science
Title of thesis:	Free-Surface Quasigeostrophy: Bridging the gap between surface quasigeostrophy and the shallow-water equations
Examining Committee:	Dr. Steven Ruuth Chair
	Dr. David Muraki Senior Supervisor
	Dr. Ralf Wittenberg
	Dr. Mary Catherine Kropinski Examiner Department of Mathematics Simon Fraser University
Date Approved:	August 8, 2003

Abstract

Observations of midlatitude vortices on the tropopause indicate that cyclones typically exhibit more intense pressure, wind and temperature perturbations than anticyclones. The primitive equations for rotating stratified flow have previously been simplified in various ways to create models which capture vortex asymmetries. Quasigeostrophic models, which represent the leading order theory in the asymptotic limit of zero Rossby number, have no vortex asymmetry. However, next-order corrections to quasigeostrophic theory have exhibited the proper asymmetry (more intense cyclones than anticyclones) when the tropopause is modeled as a flat, rigid surface. On the other hand, a study of the shallow-water primitive equations found anticyclones to be slightly more intense than cyclones; a part of this we think may be due to effects of the free-surface boundary condition.

This study attempts to reconcile these seemingly opposing results by implementing a free-surface quasigeostrophic model with next-order corrections, where the rigidity of the surface boundary condition is parameterized. The background to quasigeostrophy with next-order corrections and the shallow-water equations is presented. Next, free-surface boundary conditions are considered and the equations for free-surface quasigeostrophy are derived. Then numerical results are presented, including: convergence in the completely rigid limit of the free-surface, a characterization of cyclone and anticyclone dynamics, and an analysis of cyclone-anticyclone asymmetry for various surface rigidities using initially balanced, freely-decaying turbulence. Results indicate that the shallow-water asymmetry is not obtained even for a flexible surface, but a weakening of the cyclone-anticyclone asymmetry is observed as the surface becomes more flexible.

Acknowledgments

This thesis would not have been possible without the ideas, patience, and inspiration of David Muraki. First, his course in fluid dynamics made mathematics fun and relevant to real world phenomena. Later as my senior supervisor and advisor for course projects, he impressed upon me what it means to do real science. I owe much to both Muraki and Greg Hakim for their physical insight and access to the computer codes developed in [8].

I am also grateful to have been a part of the friendly mathematics community at SFU. In particular, the undergraduate courses I took from Rustum Choksi and Bob Russell inspired me to pursue applied mathematics as a career. The atmospheric fluid dynamics Friday seminars were always enriched by the presence of Jim Verner and Ralf Wittenberg. The applied math students and postdocs at PIMS were also very helpful in answering my many numerical, software and typesetting questions.

Finally, thanks to my family for putting up with my antics for so long, and to my friends who keep coming back for more.

Contents

List of Tables

List of Figures

Chapter 1

Introduction

1.1 Rotating, stratified fluid dynamics

Problems in atmospheric fluid dynamics typically involve scales where the effects of both rotation and stratification are important. The Earth's rotation creates the Coriolis force, which is significant when the period of rotation is comparable to the time taken to cover a length L at a speed U.[1] Therefore when

$$\epsilon = \frac{\text{period}}{\text{time to cover } L \text{ at speed } U} = \frac{2\pi/\omega}{L/U} = \frac{2\pi U}{\omega L} \tag{1.1}$$

is less than one ($\epsilon \lesssim 1$) rotation is important. If strong enough, rotation causes the flow to be vertically rigid, which is an effect known as "Taylor curtains" [5]. Stratification effects on the other hand become important when the change in potential energy due to density variation is greater than the associated kinetic energy ($\gamma \lesssim 1$)

$$\gamma = \frac{\frac{1}{2}\rho_0 U^2}{\Delta\rho g H}, \tag{1.2}$$

where $\Delta\rho$ is the change in density over height H and ρ_0 is the average density. In equilibrium, stratification creates stacked horizontal layers which make the fluid "stably stratified" because it resists vertical motion.

[1] Centrifugal forces are also created but are negligible at length (L=1000km) and velocity scales (U=10ms^{-1}) of interest, see Section 2.1.1 for more on the Coriolis force and Section 2.1.2 for typical scales.

1.2 Cyclone-anticyclone asymmetry on the tropopause

This study is concerned with vortex asymmetries on synoptic scales[2] at midlatitudes ($\alpha \approx 45°$), a regime where both rotation and stratification dominate the flow, and nonlinear effects are subtle. Vortices are persistent eddies with closed streamlines around a centre. For the purposes of this work, anticyclones (cyclones) are vortices resulting from high (low) pressure and temperature perturbations which generally rotate clockwise (counter-clockwise) in the northern hemisphere[18].

Vortices are thought to organize asymmetrically from small-scale turbulence on the "tropopause"[16], which is the boundary between the well mixed troposphere[3] (linear stratification, weak potential vorticity[4]) below and the stratosphere (strong stratification, strong potential vorticity) above. This boundary is typically identified as either the "thermal" or "dynamical" tropopause, depending on the variable of interest. The "thermal tropopause" is typically defined as the lowest height where the vertical temperature gradient is greater than -2 Kkm^{-1} while the "dynamical tropopause" is defined at a specific value of potential vorticity (Q). The concept of the dynamical tropopause is advantageous because it is a material surface since Q is conserved along particle paths in inviscid, incompressible flows[20], which means

$$\frac{DQ}{Dt} = 0. \tag{1.3}$$

Observations of vortices on the tropopause at midlatitudes indicate that cyclonic disturbances exhibit more intense pressure, wind and temperature perturbations compared to anticyclones[12],[8]. The reasons for the preferred asymmetries are not completely understood. This thesis work contributes to the understanding of vortex asymmetry by modeling the tropopause as a free-surface of constant potential vorticity.

1.3 Summary of previous studies

The physics which give rise to cyclone-anticyclone asymmetry have been studied numerically using various models for simplified versions of the primitive equations of atmospheric

[2]Weather phenomena that are 250km to 2000km across[6].

[3]The troposphere is the lowest layer of the atmosphere, ranging from the ground to a height $H \approx$10km.

[4]Potential vorticity is an exact conserved quantity in atmospheric fluid flow that is dependent on wind and temperature gradients, see Section 2.2 for its definition.

fluid flow[5]. For example, Cushman-Roisin and Tang[4] studied the emergence of eddies using a generalized geostrophic model, and Yavneh et al.[21] analyzed decaying geostrophic turbulence with a balance equation model. Both of these studies, as well as a study in the shallow-water regime by Polvani et al.[14] found larger and stronger anticyclones compared to cyclones, an asymmetry which is opposite to that observed on the tropopause. In contrast, a quasigeostrophic[6] model with next-order corrections (and therefore finite Rossby number) by Hakim et al.[8] has exhibited the correct asymmetry.

The Hakim et al. study, called sQG^{+1} which stands for surface quasigeostrophy (with next-order corrections), used the Polvani shallow-water study as a benchmark by using equivalent random initial conditions. However the shallow-water equations and sQG^{+1} are different approximations to the primitive equations. For example, the shallow-water system is comprised of a homogeneous fluid (constant density) with a kinematic free-surface representing the tropopause is effectively piecewise constant stratification (density ρ_0 below the surface and zero above). On the other hand, sQG^{+1} includes continuous (linear) stratification but assumes the height of the surface which represents the tropopause to be fixed in time. The results of [8] and [14] leave one wondering what the effect is of adding a free-surface to sQG^{+1}? Will the preferred asymmetry weaken and eventually reverse as the surface becomes more flexible? The purpose of this work is to present the theory and results of "free-surface quasigeostrophy" ($fsQG^{+1}$) simulations, with the hopes of reconciling the apparently divergent results in [14] and [8].

The $fsQG^{+1}$ model is part of a suite of tropopause models being developed by David Muraki with collaborators Greg Hakim and Chris Snyder. The evolution of these models is illustrated in Figure 1.1. Starting on the left, sQG is the original (leading-order) surface quasigeostrophy model developed by Held et al.[9] which constructed, based on theory developed by Blumen [2], a half space of uniform potential vorticity bounded by a surface. Juckes[10] argued that such a system is relevant to tropopause dynamics because the tropopause may be approximated as a discontinuity in two constant regions of potential vorticity. Typical potential vorticity values are nearly six times larger in the lower stratosphere than the troposphere[18]. The oval at the top left corner of Figure 1.1, QG^{+1}, is

[5]The full primitive equations are the Euler equations with rotation and an energy equation, detailed in Section 2.1.

[6]Quasigeostrophic models, described in Section 2.2, represent the primitive atmospheric fluid equations in the asymptotic limit where Rossby number is zero.

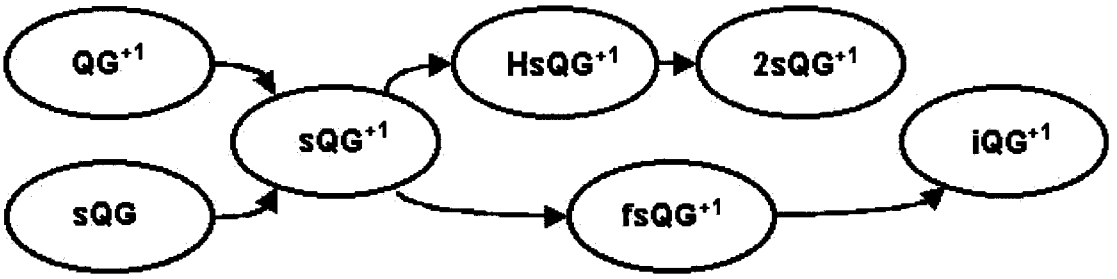

Figure 1.1: Flow chart of the sQG^{+1} research plan

the method developed by Muraki et al.[13] for next-order asymptotic corrections to quasi-geostrophy (QG), summarized in Section 2.2.2. The sQG^{+1} model in Hakim et al.[8] is a QG^{+1} version of sQG, with a fixed surface and decay below (representing the troposphere). The next-order corrections were responsible for cyclone-anticyclone asymmetry. Cyclones were more intense and had a preferred length scale while anticyclones did not. Single elliptical anticyclones tended to axisymmetrize while cyclones kept their ellipticity. Also, the fixed sQG^{+1} surface experienced mean warming as the initially random surface conditions organized into vortices.

Next in Figure 1.1, $HsQG^{+1}$ is a finite depth version of sQG^{+1}, and $2sQG^{+1}$, which stands for two surface quasigeostrophy, incorporates a ground surface. The current model, $fsQG^{+1}$, developed from sQG^{+1}, is the most like shallow-water (with infinite depth), with a fluid below the free-surface and a void, or passive fluid, above. The ultimate goal in the research plan is to develop "interface quasigeostrophy" (iQG^{+1}) which will be a true model of the tropopause with a free-interface separating two fluids that represent the troposphere and the stratosphere.

1.4 Overview of this work

This work aims to reconcile the differing conclusions about cyclone-anticyclone asymmetry between sQG^{+1} and the shallow-water equations by allowing the sQG^{+1} surface to be flexible. The flexibility of this surface is controlled by a parameter ($\sigma > 0$). Until now the phenomena associated with $fsQG^{+1}$ were unknown. This work implements a well-behaved numerical scheme for time derivative surface boundary conditions and characterizes the

dynamics of fsQG^{+1}.

The remainder of this work is comprised of five chapters. Chapter 2 reviews the primitive equations of atmospheric fluid dynamics, and outlines the theory of the shallow-water equations and sQG^{+1}, the two main sources for this work. The assumptions and their ramifications are discussed for each of these systems. Chapter 3 introduces the theory and equations for fsQG^{+1}, with emphasis on the free-surface boundary conditions. The special case of time steady axisymmetric flow is solved analytically, and the cyclone-anticyclone asymmetry is shown to reverse for a very flexible surface (small σ) in Figure 3.4.

Chapter 4 is devoted to numerical methods and issues. In the first section, spectral methods for inverting Laplace equations are discussed, and spectral convergence is shown. Section 4.2 is concerned with the time evolution of a nonlinear advection equation, where large gradients that grow at small scales must be annihilated by properly tuned hyperdiffusion. The rest of Chapter 4 deals with the creation of random initial conditions and the statistical methods used for a vortex census based on freely-decaying turbulence simulations.

Chapter 5 characterizes the organization of cyclones and anticyclones in fsQG^{+1} and discusses the results of the vortex census. Mean surface warming is also considered as a function of surface flexibility (σ). The ensemble statistics indicate that as σ decreases, the cyclone-anticyclone asymmetry is weakened, but not reversed. At $\sigma = 1$, Figure 5.5(f) shows that there is almost no asymmetry between cyclone and anticyclone radii, but cyclones are still on average slightly more intense (Figures 5.5(b) and 5.5(d)).

Finally, the project is summarized and an outline for further research is given in Chapter 6.

Chapter 2

Background: quasigeostrophy and shallow-water

2.1 Primitive equations and approximations

The primitive equations of atmospheric fluid motion are analogous to the Euler equations with rotation and stratification built-in. Instead of pressure, an equivalent (density absorbed) variable called geopotential[1], denoted by ϕ^T, is used. Also, density ρ is replaced by potential temperature[2] θ^T, which is inversely proportional to density in an ideal gas. Even though temperature decreases approximately linearly with height z in the troposphere, potential temperature increases linearly. However, at a fixed height potential temperature is a measure of temperature so cold spots ($\Delta\theta^T < 0$) are associated with heavy air, and a warm spots are associated with light air.

The following primitive equations are for an f-plane geophysical fluid system that is

[1] Geopotential is a measure of the altitude of a surface of equal atmospheric pressure at a given time[6].

[2] θ^T is defined as the temperature that a parcel of air would assume if it were brought adiabatically to the surface pressure (1 atm) [6].

adiabatic, inviscid, and Boussinesq[3] [13]:

$$\begin{aligned} u_x + v_y + w_z &= 0 \\ \frac{Du}{Dt} - fv &= -\phi_x^T \\ \frac{Dv}{Dt} + fu &= -\phi_y^T \\ \frac{Dw}{Dt} - \frac{g}{\theta^0}\theta^T &= -\phi_z^T \\ \frac{D\theta^T}{Dt} &= 0, \end{aligned} \tag{2.1}$$

where the advective (or material) derivative is defined as

$$\frac{D}{Dt} \equiv \frac{\partial}{\partial t} + u\frac{\partial}{\partial x} + v\frac{\partial}{\partial y} + w\frac{\partial}{\partial z}. \tag{2.2}$$

The constant f is the Coriolis frequency, which is defined in the next section on approximations, $\theta^0 = 300\text{K}$ is the reference potential temperature, and g is the usual gravitational acceleration. The Boussinesq approximation assumes that the relative density variations $\rho'(x, y, z, t)$ are small compared to the mean density $\rho_0(z)$ which decreases linearly with height. Therefore, the first equation in (2.1) is a Boussinesq conservation of mass statement

$$\rho = \rho_0(z) + \rho'(x, y, z, t), \qquad \rho' \ll \rho_0, \tag{2.3}$$

because the relative variations of density in time and space are typically much smaller than the relative variations of velocity. The last equation is the adiabatic statement which says potential temperature is conserved along particle paths.

2.1.1 The f-plane approximation and hydrostatic balance

To understand the f-plane terms in the primitive equations (2.1), consider what happens to the total advective derivative when rotation is included[11]:

$$\frac{D'}{Dt}(\cdot) = \frac{D}{Dt}(\cdot) + \vec{\Omega} \times (\cdot) \tag{2.4}$$

where $\vec{\Omega}$ is the angular velocity and the primed coordinates denote the inertial reference frame. Remembering that $\vec{u}'$ is just advection of $\vec{r}$, the absolute acceleration becomes

$$\begin{array}{ccccccc} \frac{D'\vec{u}'}{Dt} & = & \frac{D\vec{u}}{Dt} & + & 2\vec{\Omega} \times \vec{u} & + & \vec{\Omega} \times \vec{\Omega} \times \vec{r} \\ \text{inertial} & & \text{relative} & & \text{Coriolis} & & \text{centrifugal} \end{array} \tag{2.5}$$

[3]The f-plane approximation is explained in section2.1.1. Adiabatic means dry and without heat loss or gain in the system.

with the acceleration due to centrifugal force being negligible[5]. Next, create the f-plane by approximating the physical domain using Cartesian coordinates as shown in Figure 2.1. In the midlatitude region of Figure2.1 ($\alpha \approx 45°$) that is cut out, Ω from equation (2.5) is

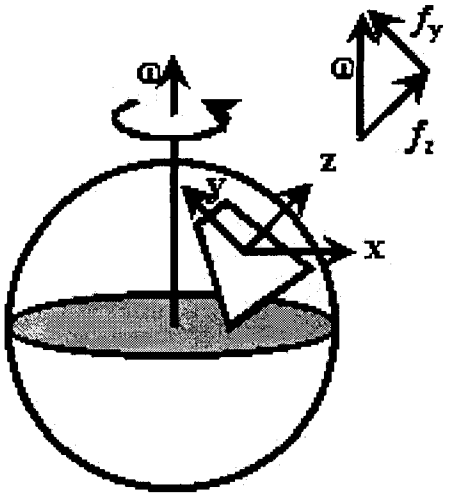

Figure 2.1: Illustration of the f-plane approximation: a local rectangular coordinate system is used to approximate the more correct spherical system.

the same as $f_z = \omega \cdot \sin\alpha$ where ω is the angular speed of the Earth, which is one rotation per day ($\omega \approx 7.3 \times 10^{-5}$rad/s). Thus the Coriolis constant in Equation (2.1) is $f \approx 10^{-4}\text{s}^{-1}$.

Another essential approximation is hydrostatic balance, which assumes that the pressure is equal to the weight of the air above in a steady (no wind) atmosphere

$$\frac{\partial p}{\partial z} = -g\rho. \tag{2.6}$$

In [13], the stratification in the troposphere is approximated as linearly decreasing density ($\rho \propto \text{const} - z$) and linearly increasing potential temperature with height. If the $\frac{Dw}{Dt}$ term in (2.1) is dropped then

$$\phi_z^T = \frac{g}{\theta^0}\theta^T. \tag{2.7}$$

Justification for neglecting $\frac{Dw}{Dt}$ is given in the next section. Finally, disturbance geopotential

ϕ and potential temperature θ are distinguished from their bulk hydrostatic parts:

$$\frac{g}{\theta^0}\theta^T = N^2 z + \frac{g}{\theta^0}\theta, \qquad \phi^T = \frac{1}{2}N^2 z^2 + \phi, \tag{2.8}$$

where N $\approx 10^{-2}s^{-1}$ is the Brunt-Väisälä frequency and superscript T denotes total ϕ or θ.

2.1.2 Nondimensional primitive equations

Nondimensionalization proceeds using the typical tropospheric, midlatitude, synoptic scales specified in Table 2.1 from [12]. The primitive variables are scaled as

$$\begin{aligned} x, y &\sim L & u, v &\sim U \\ z &\sim H & t &\sim L/U \\ \Rightarrow \phi &\sim fUL & \theta &\sim fUL/H \\ \Rightarrow w &\sim \frac{fU^2}{HN^2}, \end{aligned} \tag{2.9}$$

where the units of ϕ_y are first matched with fu, then θ is matched to ϕ_z and $N^2 w$ is matched to $\frac{D\theta}{Dt}$.

Table 2.1: Values for typical dimensional quantities and dimensionless parameters at midlatitude synoptic scales.

Dimensional quantities	Value	Dimensionless parameter	Definition	Value
L	1000km	R	$\frac{U}{fL}$	0.1
U	10ms^{-1}	B	$\left(\frac{NH}{fL}\right)^2 = \left(\frac{R}{F}\right)^2$	1
f	10^{-4}s^{-1}	δ	$\frac{U}{NL}$	0.001
N	10^{-2}s^{-1}	F	$\frac{U}{NH} = \frac{U}{\sqrt{gH}}$	0.1
H	10km			

The dimensionless primitive equations (with disturbance θ and ϕ) then become

$$\begin{aligned} u_x + v_y + \frac{R}{B}w_z &= 0 \\ R\frac{Du}{Dt} - v &= -\phi_x \\ R\frac{Dv}{Dt} + u &= -\phi_y \\ \delta^2\frac{Dw}{Dt} - \theta &= -\phi_z \quad \Rightarrow \quad \theta = \phi_z \quad (\delta^2 \ll 1) \\ \frac{D\theta}{Dt} + w &= 0, \end{aligned} \tag{2.10}$$

and the dimensionless advective derivative becomes

$$\frac{D}{Dt} \equiv \frac{\partial}{\partial t} + u\frac{\partial}{\partial x} + v\frac{\partial}{\partial y} + Rw\frac{\partial}{\partial z}, \tag{2.11}$$

where R is the Rossby number and B is the Burger number[4], as defined in Table 2.1. The Rossby number is proportional to ϵ in Equation (1.1) and $R \ll 1$ indicates that the Coriolis force is dominant in this flow regime. The parameter F is the Froude number which is proportional to γ in Equation (1.2) and $F \ll 1$ indicates that stratification is strong. The Burger number is a relative measure of the strength of rotation versus stratification; $B = 1$ means that both are important. Also, since δ^2 is negligible, the hydrostatic balance approximation is justified. The full nondimensional potential temperature and geopotential are

$$\theta^T = \frac{1}{R}z + \theta, \qquad \phi^T = \frac{1}{2}\frac{1}{R}z^2 + \phi. \tag{2.12}$$

2.2 Quasigeostrophy

Quasigeostrophy is a flow regime derived from the limit as Rossby number goes to zero ($R \to 0$). If one simply sets $R = 0$ in the nondimensionalized primitive equations (2.10) then "geostrophy" is obtained, as illustrated in Figure 2.2. Geostrophic flow is time-independent and winds (u and v) flow along contours (isobars) of geopotential ϕ, which acts as a stream-function. Notice that Ω, the projection Earth's rotation vector (ω) in the $\hat{z}$ direction of the f=plane, is in the same direction as the flow in the low pressure system, which might appear like a source for cyclone-anticyclone asymmetry. However, quasigeostrophy is known to exhibit cyclone-anticyclone symmetry [8] so the asymmetry is a next-order phenomenon.

Quasigeostrophy, developed by Charney in 1948 [3], is like geostrophy but retains time dependence via conservation of potential vorticity (Equation (1.3)) which can be derived from the primitive equations. Total potential vorticity, defined as

$$Q \equiv \left[\hat{z} + R\nabla \times \begin{pmatrix} u \\ v \\ 0 \end{pmatrix}\right] \cdot \nabla\theta^T \tag{2.13}$$

[4]Since $B \approx 1$ in the troposphere, it will be left out of most equations. If this study included a stratosphere then B would experience a jump across the tropopause.

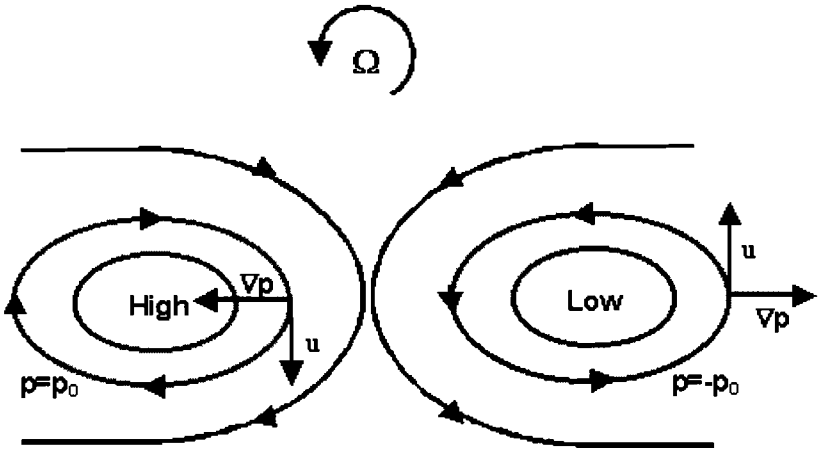

Figure 2.2: Geostrophic flow is along isobars. (Left) Anticyclonic flow is clockwise in the northern hemisphere, (right) cyclonic flow is counterclockwise which is the same as the Earth's rotation ω.

is passively advected in the flow. But only the disturbance potential vorticity[5]

$$q \equiv (v_x - u_y + \theta_z) + R\left[(v_x - u_y)\theta_z - v_z\theta_x + u_z\theta_y\right], \tag{2.14}$$

is relevant to the disturbance primitive equations in (2.10) [13].

2.2.1 Potential representation of the primitive equations

An important step in the development of sQG^{+1} is the reformulation of the momentum equations in (2.10) into a potential representation, using the Helmholtz decomposition[6][13]:

$$\begin{aligned}\begin{pmatrix} v \\ -u \\ \theta \end{pmatrix} &= \begin{pmatrix} \phi_x \\ \phi_y \\ \phi_z \end{pmatrix} + R\frac{D}{Dt}\begin{pmatrix} u \\ v \\ 0 \end{pmatrix} \\ &= \nabla\Phi + \nabla \times \begin{pmatrix} F \\ G \\ 0 \end{pmatrix} = \begin{pmatrix} \Phi_x - G_z \\ \Phi_y + F_z \\ \Phi_z + G_x - F_y \end{pmatrix},\end{aligned} \tag{2.15}$$

[5]The disturbance potential vorticity is obtained by separating the stratification of θ^T in 2.13 so that $Q = 1 + Rq$.

[6]The Helmholtz decomposition is also known as the Hodge decomposition.

where the potentials Φ, F, and G are not unique since any harmonic function ($\nabla^2 H = 0$) satisfies

$$\vec{0} = \nabla H_z + \nabla \times \begin{pmatrix} -H_y \\ H_x \\ 0 \end{pmatrix}. \tag{2.16}$$

This "harmonic ambiguity" allows flexibility in choosing boundary conditions for the potentials F and G.

Sufficient manipulation of Equation (2.15) through divergence and curl operations give the following Poisson equations that potentials must satisfy

$$\begin{aligned} \nabla^2 F &= R\left[\left(\frac{Dv}{Dt}\right)_z - \left(\frac{D\theta}{Dt}\right)_x\right] \\ \nabla^2 G &= R\left[-\left(\frac{Du}{Dt}\right)_z - \left(\frac{D\theta}{Dt}\right)_y\right] \\ \nabla^2 \Phi &= q - R\nabla \cdot \left[\theta\left(\nabla \times \begin{pmatrix} u \\ v \\ 0 \end{pmatrix}\right)\right], \end{aligned} \tag{2.17}$$

and the continuity equation in (2.10) yields the consistency statement

$$F_x + G_y = Rw. \tag{2.18}$$

2.2.2 Next-order corrections to quasigeostrophy

With the potential formulation of the primitive equations we can write the potentials and primitive variables in terms of systematic Rossby number perturbation expansions:

$$\begin{aligned} \Phi(x,y,z,t) &= \Phi^0 + R\Phi^1 + O(R^2) \\ F(x,y,z,t) &= \quad RF^1 + O(R^2) \\ G(x,y,z,t) &= \quad RG^1 + O(R^2) \end{aligned} \tag{2.19}$$

where the F and G have no leading-order terms to be consistent with (2.18). The primitive variables up to order R, except w which is only needed to leading-order, are

$$\begin{aligned} u &= u^0 + Ru^1 + \cdots = -\Phi_y^0 - R\left(\Phi_y^1 + F_z^1\right) + O(R^2) \\ v &= v^0 + Rv^1 + \cdots = \Phi_x^0 + R\left(\Phi_x^1 - G_z^1\right) + O(R^2) \\ \theta &= \theta^0 + R\theta^1 + \cdots = \Phi_z^0 + R\left(\Phi_z^1 + G_x^1 - F_y^1\right) + O(R^2) \\ w &= w^0 + \cdots = F_x^1 + G_y^1 + O(R), \end{aligned} \tag{2.20}$$

so knowing Φ^0 allows one to find leading-order θ, u, and v. Then the leading order primitive variables can be substituted into (2.17) to derive Poisson equations for each of the potentials at leading and next-order

$$\begin{aligned} \nabla^2\Phi^0 &= q^0 \\ \nabla^2\Phi^1 &= q^1 - \left(\nabla^2\Phi^0\right)\Phi_{zz}^0 + |\nabla\Phi_z^0|^2 \\ \nabla^2 F^1 &= 2J\left(\Phi_z^0, \Phi_x^0\right) \\ \nabla^2 G^1 &= 2J\left(\Phi_z^0, \Phi_y^0\right), \end{aligned} \tag{2.21}$$

where $J(f,g) \equiv f_x g_y - f_y g_x$ is the 2D Jacobian.

2.2.3 Surface quasigeostrophy (sQG^{+1})

In sQG^{+1} the problem of computing Φ^0 is easy because the potential vorticity is assumed to be uniformly zero ($q \equiv 0$). This idealization makes the total potential vorticity piecewise constant[7] as in [10]. Setting $q \equiv 0$ also simplifies the inversion of Equation (2.21) from a three-dimensional problem to a two-dimensional problem because Φ^0 becomes harmonic. The equations for Φ in (2.21) now simplify to

$$\begin{aligned} \nabla^2\Phi^0 &= 0, \\ \nabla^2\Phi^1 &= |\nabla\Phi_z^0|^2 \end{aligned} \tag{2.22}$$

and fortunately particular solutions to F^1, G^1, and Φ^1 can immediately be specified

$$F^1 = \Phi_y^0\Phi_z^0 + \tilde{F}^1, \qquad G^1 = -\Phi_x^0\Phi_z^0 + \tilde{G}^1, \qquad \Phi^1 = \frac{1}{2}\Phi_z^0\Phi_z^0 + \tilde{\Phi}^1 \tag{2.23}$$

[7] $Q = 1$ in the tropopause and nothing above. Presumably for iQG^{+1} in Figure 1.1, Q will take a value such as 6 in the stratosphere.

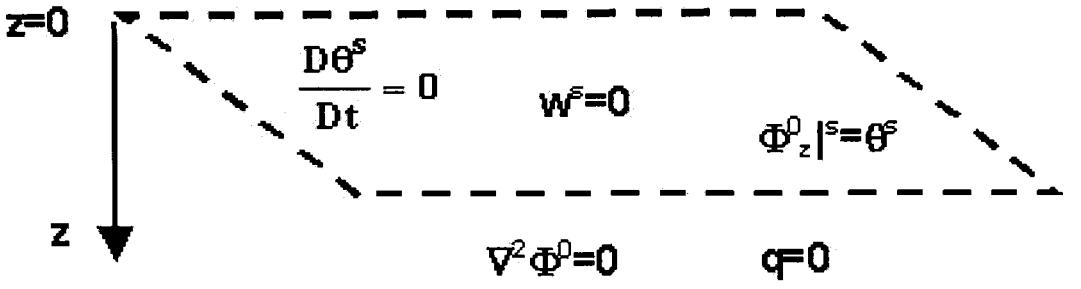

Figure 2.3: Diagram of sQG^{+1} domain and boundary conditions. The surface is at $z = 0$, dynamics decay as $z \to -\infty$, and the domain is periodic in x and y.

so that we only need to solve for the harmonic functions $\tilde{F}^1$, $\tilde{G}^1$, and $\tilde{\Phi}^1$ on the surface to solve for the next-order winds in Equation (2.20). The derivatives of the potentials are found easily using a Fourier representation. Derivatives in the vertical direction, such as F_z, are also easy to obtain since F is harmonic which means $\widehat{F_z}(k,l,t) = \sqrt{k^2+l^2}\hat{F}(k,l,t)$ in the Fourier domain.

Figure 2.3 shows the boundary conditions that completely specify the system. Potential temperature (θ_s) is specified on the surface ($z = 0$) as an initial Neumann boundary condition, which is inverted to obtain the potentials to within an arbitrary constant. The logical flow of the solution is illustrated in Figure 2.4. We compute leading and next-order winds on the surface[8] so that θ^s can be updated via advection

$$\frac{\partial \theta^s}{\partial t} = -u^s \frac{\partial \theta^s}{\partial x} - v^s \frac{\partial \theta^s}{\partial y} \qquad \Leftrightarrow \qquad \frac{\partial \theta^s}{\partial t} = N^0[\theta^s] + RN^1[\theta^s], \tag{2.24}$$

where

$$N^0[\theta^s] = -\left(u^0\theta_x + v^0\theta_y\right)\Big|^s, \qquad N^1[\theta^s] = -\left(u^1\theta_x + v^1\theta_y\right)\Big|^s, \tag{2.25}$$

are nonlinear functionals of the surface potential temperature θ^s. This system is solved using spectral methods in space and finite differences in time as described in Chapter 4. The findings of the sQG^{+1} study by Hakim et al.[8] were outlined in Section 1.3.

[8] Although in principle the winds are known throughout the 3D domain.

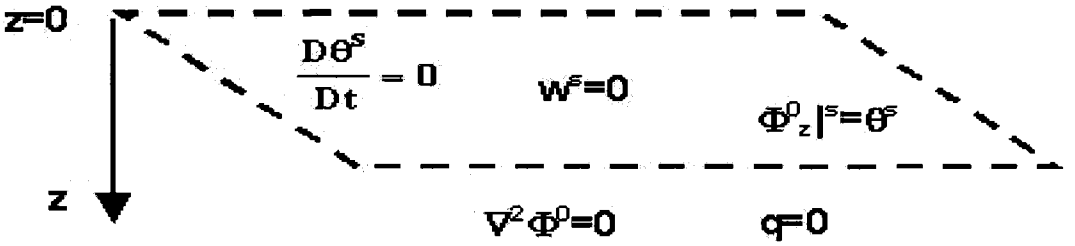

Figure 2.4: Solution flow chart for sQG^{+1}. First specify θ on the surface and invert to get Φ^0. Then compute the leading order winds and next-order potentials from Φ^0. Finally, compute nonlinear leading and next-order functionals to update θ

2.3 The shallow-water equations

The shallow-water equations are the simplest form of the equations of motion that can be used to describe the horizontal structure of the atmosphere[15]. The main assumption in the shallow-water equations is the barotropic approximation which assumes the stratification of the fluid is only piecewise-constant instead of continuously stratified as in quasigeostrophy. The only effective stratification is the jump across the free-surface. The dimensional shallow-water equations in an incompressible rotating fluid are [14]:

$$\begin{aligned} \frac{Du}{Dt} - fv &= -gh_x^* \\ \frac{Dv}{Dt} + fu &= -gh_y^* \\ \frac{Dh^*}{Dt} + h^*(u_x + v_y) &= 0, \end{aligned} \tag{2.26}$$

where h^* is the total depth of the fluid, which acts like pressure. The nondimensional shallow-water equations are:

$$\begin{aligned} R\frac{Du}{Dt} - v &= -h_x \\ R\frac{Dv}{Dt} + u &= -h_y \\ \frac{R}{B}\left(\frac{Dh}{Dt} + h(u_x + v_y)\right) + (u_x + v_y) &= 0, \end{aligned} \tag{2.27}$$

where $R << 1$ and $B \approx 1$ are the Rossby and Burger numbers as defined in Table 2.1, and h is the perturbation height defined by $h^* = H(1 + RB^{-1}h)$. A full derivation of the

shallow-water equations can be found in [15].

In the shallow-water study [14], various regions of the (R,B) parameter space were investigated. A weak bias towards anticyclones was exhibited (Fig. 11) in the most similar study (Trial B, with (R,B)=(0.05,1)) to the quasigeostrophic regime.

Chapter 3

Free-Surface Quasigeostrophy

3.1 Free-surface boundary conditions

In this chapter, the theory of sQG^{+1} is taken one step further to free-surface quasigeostrophy (fsQG^{+1}) which allows the surface to be weakly displaced. Two new conditions, reminiscent of the shallow-water boundary conditions, are specified at the surface instead of the no vertical surface flow ($w^s = 0$) condition in sQG^{+1}. First, the pressure (ϕ^T) is held fixed at zero on the free-surface since in this model there is nothing above the surface[1]. Second, a kinematic free-surface condition is applied for weak (Rossby order) displacement. These two conditions combine to make a free-surface parameter S which is the fsQG^{+1} equivalent of θ^s in sQG^{+1}.

3.1.1 Constant pressure boundary condition

Recall how total potential temperature and pressure were defined for the typical synoptic scales in Equation (2.12). The introduction of a positive constant σ in the total potential temperature acts merely as an offset and does not affect stratification. Then under hydrostatic balance ($\theta^T = \phi^T_z$),

$$\theta^T = \frac{1}{R}(z - \sigma) + \theta \quad \Rightarrow \quad \phi^T = \frac{1}{R}\left(\frac{1}{2}z^2 - \sigma z\right) + \phi, \tag{3.1}$$

where the disturbance potential temperature is still equal to the gradient of disturbance geopotential ($\theta = \phi_z$). The total pressure is still zero at $z = 0$ but now the stiffness of

[1] ϕ^T is no longer geopotential as defined earlier when $\phi^T = 0$ at $z = 0$. But it still represents a pressure like quantity with the correct stratification.

the interface is parameterized by the constant σ, as illustrated in Figure 3.1. For small σ the surface is flexible compared to large σ because in equilibrium the vertical pressure gradient at the surface ($\phi_z^T = -\sigma/R$ in steady state) is weaker[2] for small σ. Allowing weak

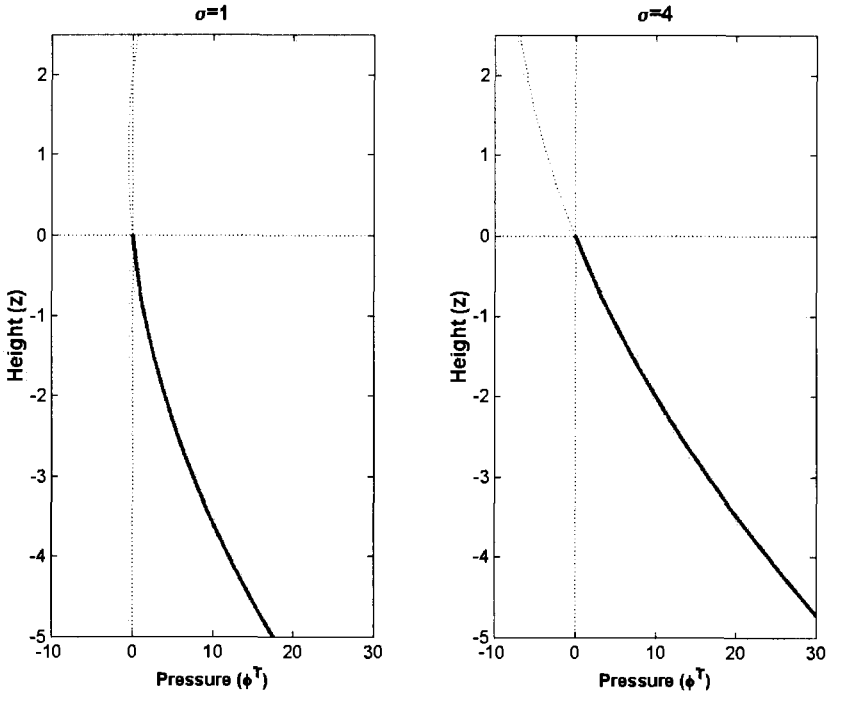

Figure 3.1: Total pressure profiles for small and large σ. When σ is small (left) the hydrostatic gradient ϕ_z^T is small just below the surface making it flexible. When σ is larger (right) ϕ_z^T is larger, making the surface heavier and more rigid.

i

displacement of the surface $z = Rh(x, y, t)$, the following zero surface pressure condition is obtained at $z = 0$ using a Taylor series:

$$\phi^T|^s = -\sigma h + \phi\,(z = 0) + R\left(\frac{1}{2}h^2 + h\phi_z(z = 0)\right) + O(R^2) = 0. \tag{3.2}$$

[2]Remember that $\phi_z = -g\rho$ in hydrostatic balance so the value of $z - \sigma$ (where $z < 0$) is proportional to density which means that large σ corresponds to heavy air.

3.1.2 Kinematic condition at free-surface

The second free-surface boundary condition is a kinematic condition found in any derivation of a free-surface, see for example [1]. Since $(z - Rh(x,y,t))|^s = 0$ it is clear that

$$\frac{D}{Dt}(z - Rh)|^s = R(w - h_t - u^s h_x - v^s h_y) = 0, \tag{3.3}$$

where w is the vertical velocity which comes from advecting z using Equation (2.11). This motivates the definition of a dynamical surface quantity

$$S \equiv \theta^T(x,y,z = Rh(x,y,t),t) = h + \theta^s(x,y,z = Rh,t) + \text{constant} \tag{3.4}$$

which is the fsQG^{+1} analogue of $\theta^s(x,y,z=0,t)$ in sQG^{+1}. Advection of S is

$$\begin{aligned}\frac{DS}{Dt} &= \frac{D}{Dt}\left(\frac{1}{R}(Rh(x,y,t) - \sigma) + \theta(x,y,z = Rh(x,y,t),t)\right), \\ &= \frac{Dh}{Dt} + (\theta_t + u\theta_x + v\theta_y)|^s + R\theta_z^s(h_t + uh_x + vh_y)\end{aligned}$$

using Equation (3.3). This expression reduces to zero as follows

$$\begin{aligned}\frac{DS}{Dt} &= \frac{Dh}{Dt} + \frac{D\theta}{Dt}\bigg|^s + R\theta_z^s\left(\frac{Dh}{Dt} - w^s\right) \\ &= \frac{Dh}{Dt} - w^s = 0,\end{aligned} \tag{3.5}$$

because $\frac{D\theta}{Dt} + w = 0$ everywhere from (2.10) and $\frac{Dh}{Dt} = w^s$ from (3.3)

3.2 Potential vorticity inversion

In sQG^{+1} the problem, illustrated in Figures 2.3 and 2.4, was to invert $q \equiv 0$ to obtain the potentials given some θ^s on the surface, and then compute the winds and advect θ^s. The inversion with θ^s represented a Laplace problem with Neumann boundary conditions. The problem in fsQG^{+1} is to invert potential vorticity subject to the new free-surface conditions which result in a Robin boundary condition.

As with sQG^{+1}, the physical variables and potentials are expanded as power series in Rossby number to perform the potential vorticity inversion order-by-order. But now the new height variable h and θ must be expanded also:

$$\begin{aligned}h &= h^0 + Rh^1 + O(R^2) \\ \theta &= \Phi_z + G_x - F_y \sim \left(\Phi^0 + R\Phi^1 + \cdots\right)_z + \left(RG^1 + \cdots\right)_x - \left(RF^1 + \cdots\right)_y.\end{aligned} \tag{3.6}$$

Expanding S as a Taylor series about $z = 0$, then substituting the expansions in (3.6) gives

$$S = h + \theta^s(x, y, z = Rh, t) = h + \theta(z = 0) + Rh\theta_z z = 0) + \frac{1}{2}R^2h^2\theta_{zz}(z = 0) + \cdots$$
$$S = h^0 + \Phi^0_z + R(h^1 + \Phi^1_z + G^1_x - F^1_y + h^0\Phi^0_{zz}) + O(R^2). \tag{3.7}$$

and the total pressure at the surface (3.2) is

$$\phi^T|^s = -\sigma h^0 + \Phi^0 + R\left(\frac{1}{2}(h^0)^2 - \sigma h^1 + \phi^1 + h^0\Phi^0_z\right) + O(R^2) = 0. \tag{3.8}$$

3.2.1 Leading order inversion (fsQG)

At leading-order the height is proportional to pressure

$$h^0 = \frac{1}{\sigma}\Phi^0(z = 0). \tag{3.9}$$

because the constant pressure boundary condition (3.2) forces total pressure to be zero. Therefore (3.7) gives a Robin boundary condition on Φ^0 if S is specified at the free-surface:

$$\begin{cases} \nabla^2\Phi^0 = 0 \\ \frac{1}{\sigma}\Phi^0\,(z = 0) + \Phi^0_z\,(z = 0) = S \\ \text{decay}\,(z \to -\infty)\,,\ \text{periodicity in}\ (x, y). \end{cases} \tag{3.10}$$

This situation is illustrated in Figure 3.2, and is solved using Fourier Transforms which are described in the next section.

3.2.2 Next-order inversion (fsQG^{+1})

The essential step in the next-order fsQG^{+1} inversion is defining a convenient condition (harmonic ambiguity) on F and G so that they can be uniquely solved. The most convenient condition is

$$\tilde{G}^1_x - \tilde{F}^1_y = 0 \tag{3.11}$$

which allows one to solve for $\tilde{\Phi}^1$ from (2.23) using the next-order conditions on S and $\phi^T|^s$ from (3.7) and (3.8) respectively

$$h^1 + \Phi^1_z + G^1_x - F^1_y + h^0\Phi^0_{zz} = 0$$
$$\frac{1}{2}(h^0)^2 - \sigma h^1 + \Phi^1 + \frac{1}{2}(\Phi^0_z\Phi^0_z - \Phi^0_x\Phi^0_x - \Phi^0_y\Phi^0_y) + h^0\Phi^0_z = 0. \tag{3.12}$$

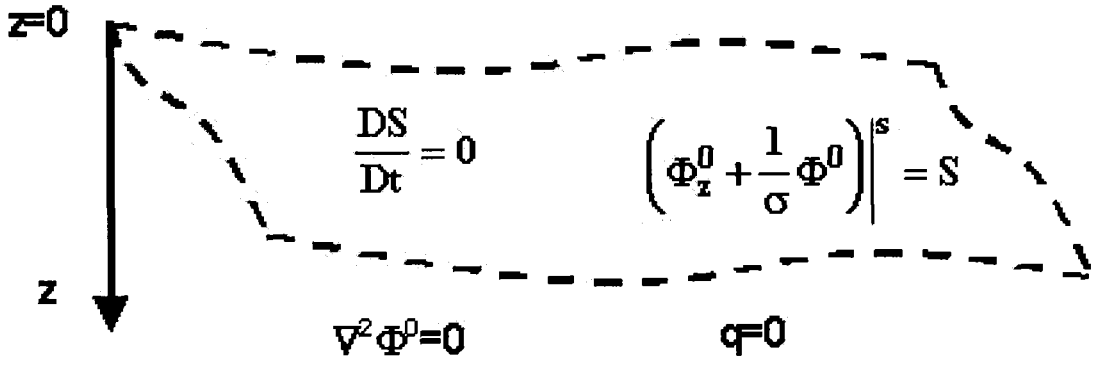

Figure 3.2: Diagram of fsQG^{+1} domain and boundary conditions. The surface is at $z = Rh$, dynamics decay as $z \to -\infty$, and the domain is periodic in x and y.

Together these conditions form a Robin boundary condition for the Laplace problem of $\tilde{\Phi}^1$. The potentials $\tilde{F}^1$ and $\tilde{G}^1$ are found using (3.11) and (2.18). For full details of the next-order fsQG^{+1} inversion, including the application of the harmonic ambiguity and the evaluation of w^0, please see Appendix A.

The solution logic for fsQG^{+1} is shown in Figure 3.3 and is analogous to Figure 2.4 for sQG^{+1}. The surface dynamical quantity S is updated via advection and the leading and

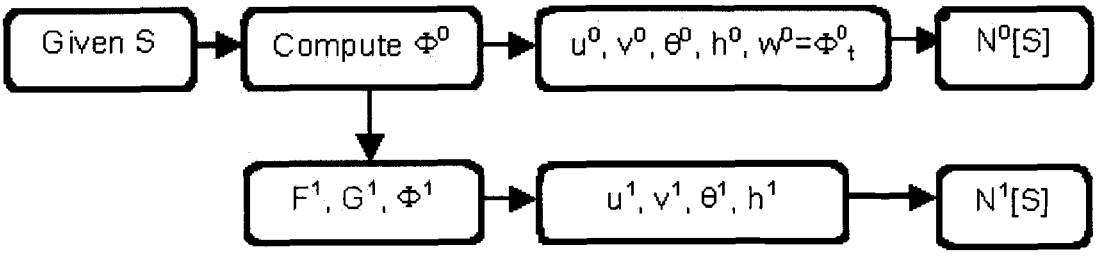

Figure 3.3: Solution flow chart for fsQG^{+1}. First specify S on the surface and invert to get Φ^0. Then compute the leading order winds and next-order potentials from Φ^0. Finally, compute nonlinear leading and next-order functionals to update S

next-order winds form nonlinear functionals of S when multiplied by the spatial derivatives

of S.

$$\frac{\partial S}{\partial t} = -u^s \frac{\partial S}{\partial x} - v^s \frac{\partial S}{\partial y} \qquad \Leftrightarrow \qquad \frac{\partial S}{\partial t} = N^0[S] + RN^1[S], \tag{3.13}$$

where

$$N^0[S] = -\left(u^0 S_x + v^0 S_y\right), \qquad N^1[\theta^s] = -\left(u^1 S_x + v^1 S_y\right), \tag{3.14}$$

are nonlinear functionals of the surface parameter S. In practice, an initial S is specified, the Fourier Transform is used for the inversion of potential vorticity, then S is updated using time differencing with the derivative in (3.13). The salient details of these calculations are described in Chapter 4.

3.3 Axisymmetric Free-Surface Quasigeostrophy

The first fsQG^{+1} model was implemented in MATLAB to solve problems involving axisymmetric S boundary conditions. The case where S is axisymmetric is time-independent, which is shown in detail in Appendix B. The time-independence argument relies on the linearity (and no dependence in the azimuthal direction) of the Φ inversions.

The axisymmetric model was useful in three ways. First, as a quick and easy to build model, it gave preliminary results which showed that the theory was correct and that development of a time-dependent model would be worthwhile. Second, until the axisymmetric model was developed, the harmonic ambiguity (2.16) in the potential representation of the primitive equations had not been independently verified. That is, the sQG^{+1} model enforced one condition on F and G but did not show that the condition was not unique. A convergence test in the limit $1/\sigma \to 0$ (Section 4.1.2) later showed that the time-dependent fsQG^{+1} model was equivalent to sQG^{+1} in this limit. Third, the axisymmetric model acted as a sanity check to ensure the time-dependent code was working properly. A plot in Section 4.1.1 illustrates the match between the three-dimensional time-dependent code and the two-dimensional time-independent code.

The boundary value problem in (3.10) has the following Hankel Transform[3] solution in polar coordinates when S is radially symmetric

$$\Phi^0(r,z) = \int_0^\infty \frac{m}{m+\frac{1}{\sigma}} \hat{S}(m) J_0(mr) e^{mz}\, dm. \tag{3.15}$$

[3]Properties and numerical implementation details of the Hankel Transform are given in Section 4.1.1.

where $J_0(\cdot)$ is the Bessel function of the first kind and zeroth order [17]. The derivation of the next-order potentials, winds, and potential temperature is explained in Appendix B.

The key results of the axisymmetric fsQG^{+1} code are shown in Figure 3.4. Plots of h compared with h^0 are shown for a Gaussian surface ($S = e^{-r^2}$) and two σ values (0.25 and 4). The top plots correspond to a positive disturbance, as in a high pressure system, and the bottom plots correspond to an equivalent low pressure system. Since cyclone-anticyclone asymmetry comes from the next-order corrections [8], the left and right plots in Figure 3.4 make it clear that the next-order contribution is reversed as σ goes from 0.25 (flexible) to 4 (rigid). This plot indicates that, at least for a single gaussian shaped vortex, the cyclone-anticyclone asymmetry observed in the Hakim et al. study [8] is reversible if the surface is made sufficiently flexible.

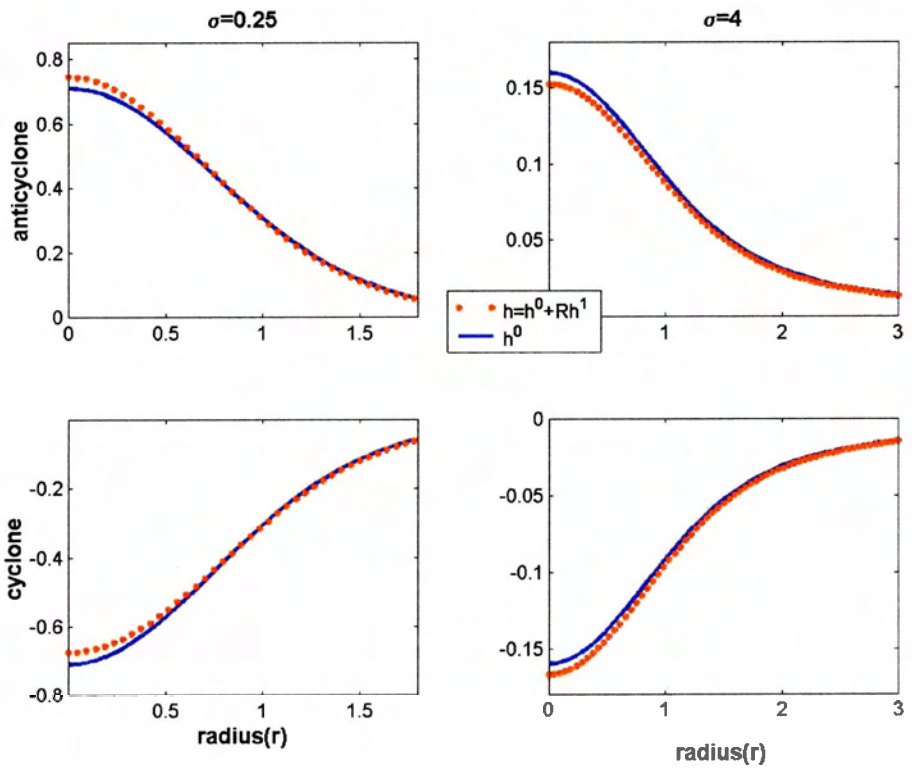

Figure 3.4: Axisymmetric inversion for positive and negative Gaussian surface values ($S = \pm e^{-r^2}$). Plots show $h = h^0 + Rh^1$ (dotted) and h^0 as a function of radius for σ=0.25 and σ=4. For small σ (left) the shallow-water asymmetry is shown, for large σ (right) the sQG^{+1} asymmetry is shown.

Chapter 4

Implementation of fsQG^{+1}

The time-dependent fsQG^{+1} model was implemented numerically in Fortran 90. Initial conditions (described in Section 4.3) and post-processing plotting routines were performed with MATLAB. This chapter describes some of the key issues and numerical techniques required to solve the fsQG^{+1} equations. The first section outlines spectral inversion of Laplace problems such as in (3.10) and presents plots that show equivalence between the axisymmetric solution and the time-dependent solution as well as convergence of sQG^{+1} to fsQG^{+1} when $\sigma \to \infty$. The second section details how to maintain numerical stability when the system contains an intrinsic small-scale energy cascade. The final two sections briefly mention how the random initial conditions were created for the freely-decaying turbulence simulations, and how the resulting vortex census data was captured.

4.1 Spectral inversion

4.1.1 Integral Transforms

Equation (3.10) is easily solved using the Fourier Transform [17],

$$\Phi^0(x,y,z,t) = \frac{1}{4\pi^2} \iint_{-\infty}^{\infty} \frac{1}{m + \frac{1}{\sigma}} \hat{S}(k,l,t) e^{i(kx+ly)} e^{mz}\, dkdl \tag{4.1}$$

where $m = \sqrt{k^2 + l^2}$ for consistency with $\nabla^2 \Phi^0 = 0$, and $\hat{S}$ is the Fourier Transform of S

$$\hat{S}(k,l,t) = \int_{-\infty}^{\infty} S(x,y,t) e^{-i(kx+ly)}\, dxdy. \tag{4.2}$$

The properties of the Fourier Transform mean that derivatives of Φ^0 are easy to obtain

$$\Phi^0_x = \frac{1}{4\pi^2}\int_{-\infty}^{\infty} \frac{ik}{m+\frac{1}{\sigma}}\hat{S}e^{i(kx+ly)}e^{mz}\,dkdl$$
$$\Phi^0_z = \frac{1}{4\pi^2}\int_{-\infty}^{\infty} \frac{m}{m+\frac{1}{\sigma}}\hat{S}e^{i(kx+ly)}e^{mz}\,dkdl. \tag{4.3}$$

In practice, the Discrete Fourier Transform was used to evaluate the above integrals with 256×256 points on the domain $x, y \in [-7\pi+14\pi/256, 7\pi]$ and $k, l \in [-128/7+1/7, 128/7]$.[1]

In the axisymmetric case, the Laplace equation $\frac{1}{r}(r\Phi^0_r)_r + \Phi^0_{zz} = 0$ has

$$\Phi^0(r,z) = \int_0^{\infty} \hat{A}(m)J_0(mr)e^{mz}\,dm \tag{4.4}$$

as its general solution given the decay condition, where J_0 is the Bessel function of the first kind and order zero [17]. The function $\hat{A}(m)$ is determined using the Robin boundary condition involving S and Φ^0. The Hankel Transform of order zero and its inverse are defined for $S(r)$ as

$$\hat{S}(m) = \int_0^{\infty} S(r)J_0(mr)r\,dr \quad \Leftrightarrow \quad S(r) = \int_0^{\infty} \hat{S}(m)J_0(mr)m\,dm, \tag{4.5}$$

so the solution $\Phi^0(r,z)$ is given by

$$\Phi^0_z + \frac{1}{\sigma}\Phi^0 = S \quad \Rightarrow \quad \hat{A}(m) = \frac{m}{m+1/\sigma}\hat{S}(m)$$
$$\Rightarrow \Phi^0(r,z) = \int_0^{\infty} \frac{m}{m+1/\sigma}\hat{S}(m)J_0(mr)e^{mz}\,dm. \tag{4.6}$$

As with the Fourier Transform derivatives of Φ^0 are easily obtained

$$\Phi^0_z(r,z) = \int_0^{\infty} \frac{m^2}{m+1/\sigma}\hat{S}(m)J_0(mr)e^{mz}\,dm,$$
$$\Phi^0_r(r,z) = \int_0^{\infty} \frac{-m^2}{m+1/\sigma}\hat{S}(m)J_1(mr)e^{mz}\,dm. \tag{4.7}$$

The integrals in (4.6) and (4.7) were summed in MATLAB using Simpson's Rule. The Gaussian disturbance ($S = e^{-\mu r^2}$) used in Figure 3.4 is particularly helpful in debugging the numerics because the Hankel transform of a Gaussian is well known

$$e^{-\mu r^2} = \int_0^{\infty} \frac{1}{2\mu}e^{\frac{-m^2}{4\mu}}J_0(mr)m\,dm. \tag{4.8}$$

Figure 4.1 shows the match between the Hankel Transform based inversion and the Fourier Transform based inversion for a single plateau ($S = \pm(1-\tanh(r^2-2)/2)$) disturbance.

[1] Note that it is important to remember to always zero the Nyquist frequency (wavenumber $k = \pi/\Delta x$) when taking spectral derivatives, and to zero pad the Fourier domain (to twice its original length and width) when multiplying terms to ensure aliasing does not occur.

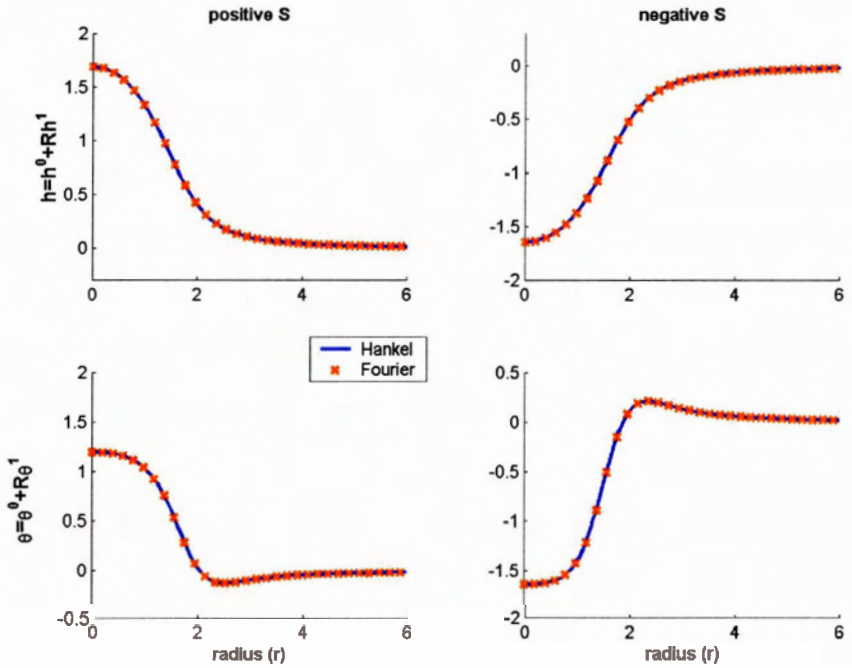

Figure 4.1: Sanity check comparison between the time-dependent Fortran code which uses the Fourier Transform and the time-independent axisymmetric Matlab code that uses the Hankel Transform. In all plots, $\sigma = 1$ and the free-surface boundary condition is a "plateau" $S = \pm(1-\tanh(r^2-2)/2)$.

4.1.2 Convergence studies

To ensure the implementation of fsQG^{+1} was correct, two convergence studies were performed. The first showed spectral convergence in the difference between sQG^{+1} and fsQG^{+1} in the limit $\sigma \to \infty$ as the number of grid points was increased[2]. The results of this study are shown in Figure 4.2 which shows semi-log plots of the maximum and root mean square (RMS) errors between the next-order winds in fsQG^{+1} and sQG^{+1}.[3] The RMS error for u^1

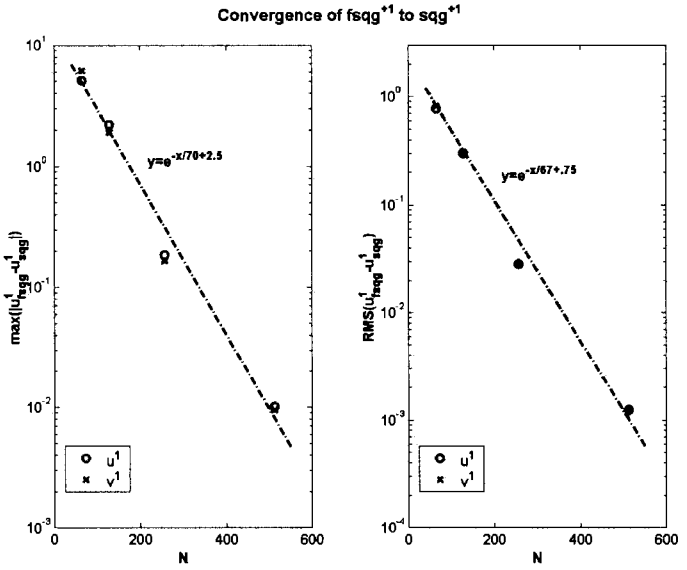

Figure 4.2: Convergence of an fsQG^{+1} ($\sigma \to \infty$) inversion to an sQG^{+1} inversion as the grid is refined. (Left) Convergence of the maximum error, (right) convergence of the RMS error.

(and v^1) is determined using

$$\sum_{k=1}^{n} RMS(u^1_{fsqg} - u^1_{sqg}) = \sqrt{\frac{\sum_{i,j=1,1}^{N,N} (u^1_{fsqg} - u^1_{sqg})^2}{N^2}}. \tag{4.9}$$

The second convergence study showed the fsQG^{+1} inversion (with $\sigma = 2$) is spectrally accurate by comparing errors between coarse grid inversions and a fine grid (N=512) inversion.

[2]The limit $\sigma \to \infty$ is realized by setting $1/\sigma = 0$.

[3]Note that these errors get multiplied by $R = 0.1$ in the next-order corrected winds $u = u^0 + Ru^1$, $v = v^0 + Rv^1$.

The results of this study are shown in Figure 4.3 as semilog plots of maximum and RMS errors.

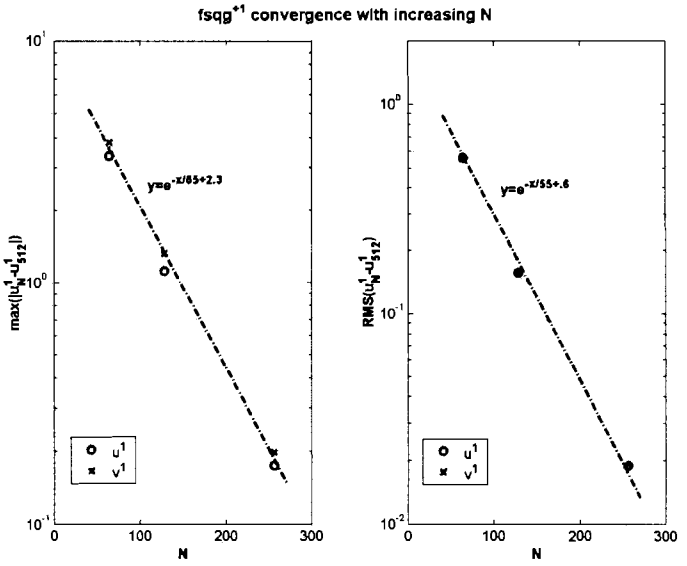

Figure 4.3: Convergence of an fsQG^{+1} ($\sigma = 2$) inversion as the grid is refined. Errors are computed by comparing with the most refined grid (N=512). (Left) Convergence of the maximum error, (right) convergence of the RMS error.

4.2 Time evolution with hyperdiffusion

In the freely-decaying turbulence simulations used for the vortex census, potential temperature θ is known to cascade down-scale with a $|\vec{k}|^{-5/3}$ energy spectrum, where $|\vec{k}| = \sqrt{k^2 + l^2}$ is the horizontal wavenumber[4] [2]. This down-scale cascade tends towards grid scale spacing and must be dissipated to ensure numerical stability. Typically horizontal "hyperdiffusion" is added to the time stepping scheme to kill off any high wavenumber components that develop.

Consider the effect of diffusion in the two-dimensional heat equation $g_t = \nu \nabla^2 g$. In Fourier space, the equation becomes $\hat{g}_t + \nu(k^2 + l^2)\hat{g} = 0$, which gives exponential decay

[4]Wavenumber is the magnitude of the wave vector $\vec{k}$ and is inversely proportional to wavelength ($|\vec{k}| = 2\pi/\lambda$).

$\hat{g}(t) = e^{-\nu(k^2+l^2)t}\widehat{g(0)}$ that is dependent on wavenumber: higher wavenumber components are dissipated faster. Hyperdiffusion ($-\nabla^8$) behaves the same, but because the exponent (n=8) is so large, it has almost no effect on low wavenumber components when the diffusion constant ν is sufficiently small.

In the main vortex census the diffusion constant was[5]

$$\nu = \frac{1}{(k_{max}^2 + l_{max}^2)^4 \Delta t/2} = 10^{-9}. \tag{4.10}$$

With a 256x256 grid and domain from -7π to 7π, k_{max} and l_{max} were both 128/7. Figure 4.4 shows the regions in the Fourier domain that are most affected by the hyperdiffusion. An example of the Fourier spectrum of θ is shown in Figure 4.5, indicating that the hyper-

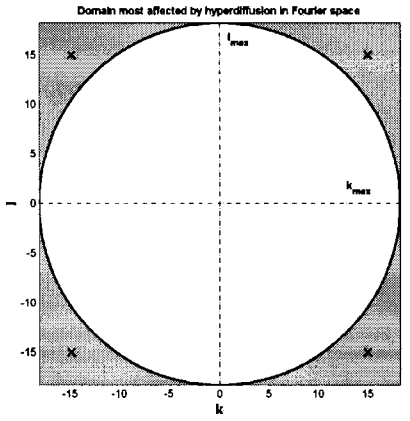

Figure 4.4: Fourier space showing regions (shaded and marked with x's) where hyperdiffusion acts most to kill off high wavenumbers.

diffusion ($\nu = 10^{-9}$) starts to affect the $k^{-5/3}$ down-scale cascade at about $|\vec{k}| = 13.3$. The dashed vertical line on the right shows $k_{max} = \pi/\Delta x$, the largest wavenumber that can be resolved by the grid.

The time derivative of S is approximated via advection with added hyperdiffusion:

$$\hat{S}_t = (-\widehat{uS_x - vS_y}) - \nu(k^2 + l^2)^4 \hat{S}. \tag{4.11}$$

[5]This is the same amount of hyperdiffusion that was used in [8] and [14].

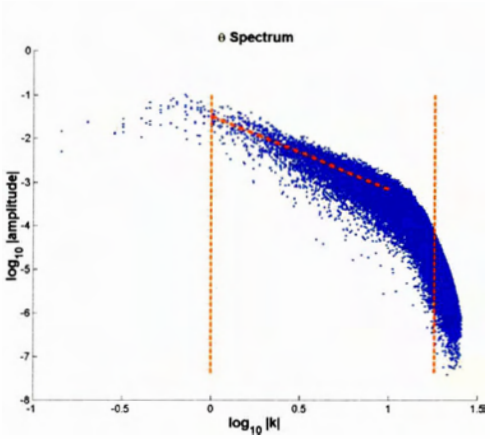

Figure 4.5: Example scatterplot of Fourier spectrum of θ, showing the effect of hyperdiffusion on high wavenumbers (with $\nu = 10^{-9}$). The dashed line on the right shows k_{max}. The diagonal line identifies the region of the $k^{-5/3}$ down-scale cascade in θ. The effect of hyperdiffusion is noticeable at $|k| > 10$.

To solve this equation, the integrating factor $e^{\nu(k^2+l^2)^4 t}$ is multiplied:

$$\left[e^{\nu(k^2+l^2)^4 t}\hat{S}\right]_t = e^{\nu(k^2+l^2)^4 t}(-\widehat{uS_x - vS_y}), \tag{4.12}$$

so that the time stepping scheme updates the variable $\psi = e^{\nu(k^2+l^2)^4 \Delta t}\hat{S}$ using a third-order Adams-Bashforth method[7]:

$$\psi^{n+1} = \psi^n + \frac{\Delta t}{12}\left[23F(\psi^n) - 16F(\psi^{n-1}) + 5F(\psi^{n-2})\right], \tag{4.13}$$

where the time step was $\Delta t = 0.01$. For the first two time steps, forward Euler time stepping is used.

The main census was performed with $\sigma = 4$ and $\sigma \to \infty$ (34 freely-decaying turbulence simulations each). A mini-census was also performed with $\nu = 10^{-8}$ for $\sigma = 10$, $\sigma = 4$ and $\sigma = 1$ (7 turbulence simulations each for $\sigma = 10$ and $\sigma = 4$, and 17 simulations for $\sigma = 1$). The mini-census was run as a backup with ample diffusion ($\nu = 10^{-8}$) to ensure stability. Although the simulations with $\nu = 10^{-8}$ appear faded (or "washed out"), the $\sigma = 1$ results (Section 5.2) show the most symmetry.

4.3 Random initial conditions for decaying turbulence

Decaying turbulence simulations are given random initial surface conditions, which are then released to allow coherent structures to develop naturally. The fsQG^{+1} initial conditions are identical to those used in [14] and [8]. The desired kinetic energy spectrum is chosen to peak at a particular scale ($|\vec{k}_0| = \sqrt{k_0^2 + l_0^2}$) using:

$$E_K(k,l) \sim \frac{m^{M/2}}{(m+k_0)^M} \tag{4.14}$$

where $M = 25$ is a constant and $m = \sqrt{k^2 + l^2}$. Then the leading-order pressure is constructed using $\frac{1}{2}m^2|\widehat{\Phi^0}(k,l)|^2 = E_K(k,l)$,

$$|\widehat{\Phi^0}(k,l)| = \frac{m^{M/4-1}}{(m+k_0)^{M/2}} \tag{4.15}$$

which gives the (yet to be normalized) Fourier spectrum in Figure 4.6. The initial conditions

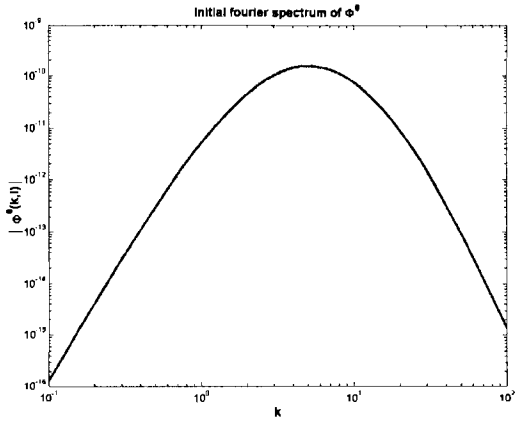

Figure 4.6: Fourier spectrum of initial $|\hat{\Phi}^0|$ with $k_0 = 7$ and $M = 25$.

are made random by giving $\hat{\Phi}^0$ random phase, and then normalizing with respect to RMS leading-order winds ($\sqrt{\sum((u^0)^2 + (v^0)^2)/N^2}$).

4.4 Capturing vortex census data

The Hakim et al. [8] sQG^{+1} census algorithm was used, with minor fsQG^{+1} modifications, to capture vortex amplitude and radius data from the ensemble of freely-decaying turbulence

simulations. The first stage of the algorithm searches the surface S values for cyclones and anticyclones. Candidates must have four properties to be considered vortices:

1. All points in the vortex must be greater (in magnitude) than some threshold above or below the mean surface value ($|S_{ij} - \bar{S}| > S_{min}$) This criterion filters vortices that are too weak.

2. The diameter of the region where $|S_{ij} - \bar{S}| > S_{min}$ (measured along 8 radial arms from the central maximum) must be greater than some minimum threshold. This criterion filters vortices that are too small.

3. The center of mass of the region $|S_{ij} - \bar{S}| > S_{min}$ must be within a certain distance of the maximum S value in the region. This criterion filters colliding or merging vortices.

4. The aspect ratio between the major and minor axes must be less than some threshold to filter out filaments.

Vortex radii are computed by taking a box around a vortex maximum with dimensions proportional to the minimum of the 8 radial arms. The center of mass of this box is then computed using

$$\bar{x} = \frac{\sum x_{ij} S_{ij}}{\sum S_{ij}}, \qquad \bar{y} = \frac{\sum y_{ij} S_{ij}}{\sum S_{ij}}. \tag{4.16}$$

Finally, the radius is taken as the square root of the minimum eigenvalue (minor axis) of the covariance matrix $M = XX^T/(\sum S_{ij})$, where X is a $2 \times N$ deviation matrix for each of the N points in the box:

$$X = \sqrt{S_{ij}} \begin{bmatrix} x_{ij} - \bar{x} \\ y_{ij} - \bar{y} \end{bmatrix} \tag{4.17}$$

The results of the census algorithm are shown for a single simulation in Figure 4.7 with captured vortices highlighted (dashed circles which show the captured radius for each vortex). Rejected vortices are encircled by faint dashed lines.

Normalization is vital when comparing simulations with different values of σ. In the sQG^{+1} model, leading-order winds are a consistent scaling measure because the root mean square of u^0 and v^0 scale with RMS(θ^0). This relation is derived using the leading-order definitions ($u^0 = -\Phi^0_y$, $v^0 = \Phi^0_x$, and $\theta^0 = \Phi^0_z$), the fact that Φ^0 is harmonic, and Parseval's

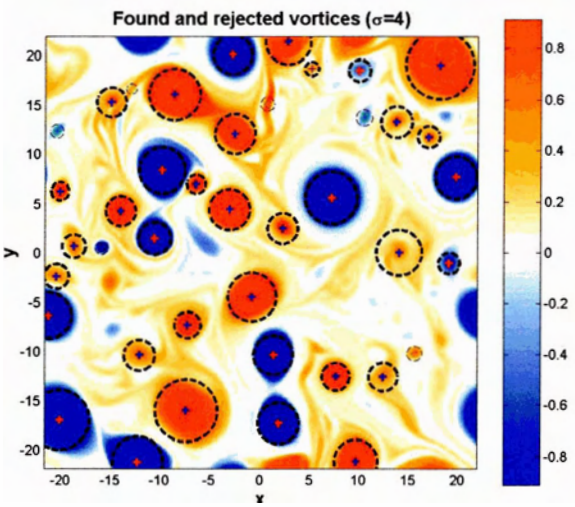

Figure 4.7: Example of vortices captured at t=500 in freely-decaying turbulence run ($\sigma = 4$ and diffusion constant $= 1 \times 10^{-8}$).

equality [19]:

$$\begin{aligned}
&\sqrt{2\pi}\|\theta^0\|_2 = \|\widehat{\theta^0}\|_2 \\
\Rightarrow &\int |\theta^0|^2 \sim \int |\widehat{\Phi_z^0}|^2 \\
&\sim \int (k^2+l^2)|\widehat{\Phi^0}|^2 = \int |k\widehat{\Phi^0}|^2 + |l\widehat{\Phi^0}|^2 \\
&\sim \int |\widehat{v^0}|^2 + |\widehat{u^0}|^2 \\
&\sim \int |v^0|^2 + |u^0|^2 \,. \qquad (4.18)
\end{aligned}$$

However, S does not scale with leading-order winds: as σ changes so does RMS(S). As a result census amplitude data increases as σ decreases unless the data is re-normalized[6]. No obvious scaling for S as a function of σ was found so the relation was determined statistically by computing RMS(S) for a set of initial conditions over σ ranging from [0.5,∞). The

[6]Normalizing by wind is still useful for comparing surface warming versus σ, which is analyzed in Section 5.3

statistical mean of RMS(S) for each σ is plotted in Figure 4.8, from which it is clear that RMS(S) scales as $1 + 0.82/\sigma$. The standard deviations of RMS(S) at each value of σ was negligible.

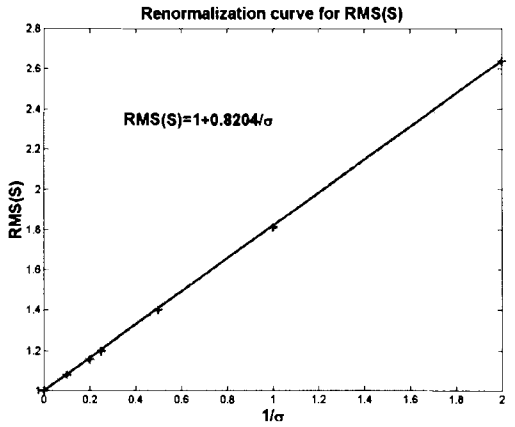

Figure 4.8: Re-normalization curve for S. The initial conditions are normalized using $\sqrt{(u^0)^2 + (v^0)^2}$ which is a θ normalization and works only for $1/\sigma = 0$. For finite σ census amplitudes, S data is re-normalized with this curve.

Chapter 5

Numerical results

5.1 Characterisation of vortex structure

In this section the structure and dynamics of cyclones and anticyclones are analyzed. Visual observations of single cyclonic and anticyclonic disturbances are made in Section 5.1.1. In Section 5.1.2 the statistics of the vortex census are presented. The census data is then plotted in Section 5.2 which discusses cyclone-anticyclone asymmetry in fsQG^{+1}.

5.1.1 Single vortex dynamics

Figure 5.1 illustrates the structure of single cyclones and anticyclones for different σ values (including $\sigma \to \infty$ which is sQG^{+1}). Notice how anticyclones retain their tails while cyclones do not because cyclones are cold anomalies and cold air sinks, breaking the tail. Also, the tendency for anticyclones to axisymmetrize is stronger than for cyclones, which prefer larger aspect ratios even as σ becomes small. Note that when anticyclones axisymmetrize, their rate of rotation increases compared to cyclones (although this effect is not visible in Figure 5.1). In the shallow-water regime, cyclones tend to axisymmetrize, which indicates that fsQG^{+1} does not tend exactly to the shallow-water equations in the limit of small σ.

Even though both the fsQG^{+1} and sQG^{+1} vortices are normalized so that the maximum winds are the same, the fsQG^{+1} vortices rotate slower than the sQG^{+1} vortices because in fsQG^{+1} part of the kinetic energy is transferred to potential energy. In fsQG^{+1} the surface is allowed to move, and raising or lowering it requires energy because of buoyancy. The situation is illustrated in Figure 5.2, where potential temperature disturbances are added

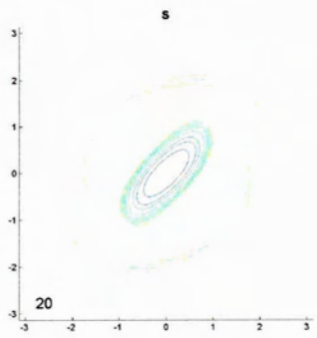

(a) $\sigma \to \infty$: cyclone

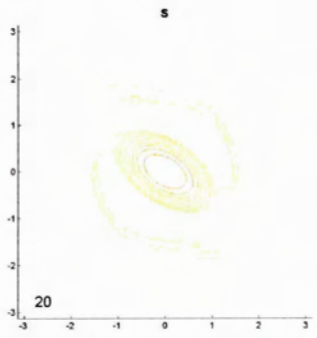

(b) $\sigma \to \infty$: anticyclone

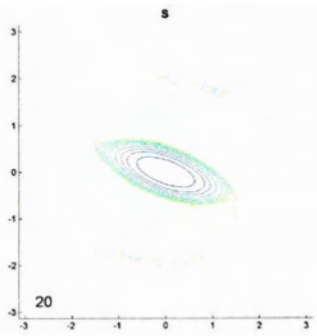

(c) $\sigma = 2$: cyclone

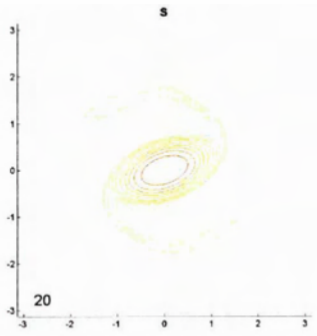

(d) $\sigma = 2$: anticyclone

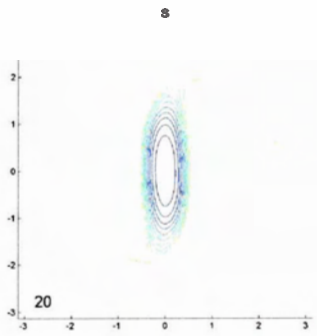

(e) $\sigma = 1/2$: cyclone

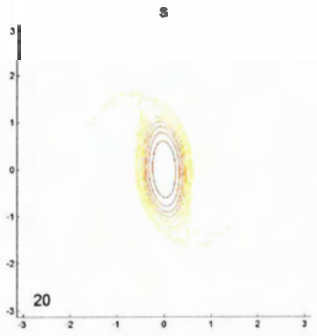

(f) $\sigma = 1/2$: anticyclone

Figure 5.1: Plots of next-order corrected S at $t = 20$ for single cyclones (left) and anticyclones (right). (Top) sQG^{+1} ($\sigma \to \infty$) at 5/8 of a rotation. (Middle) fsQG^{+1} ($\sigma = 2$) at 3/8 rotation. (Bottom) fsQG^{+1} ($\sigma = 1/2$) at 1/4 rotation. Color axis scaling for all plots is from -2 (blue) to 2 (red).

to the base hydrostatic system. The movement of the fsQG^{+1} surface has the effect of

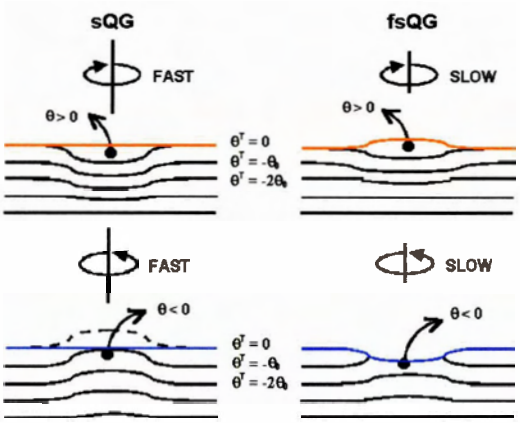

Figure 5.2: Illustration of potential temperature disturbances on the surface for sQG (left) and fsQG (right). The horizontal lines are lines of constant total potential temperature θ^T. For both anticyclones (top) and cyclones (bottom), fsQG surface motion weakens the θ_z gradient, so fsQG vortices rotate slower than sQG vortices.

lengthening both cyclonic and anticyclonic disturbances so the θ_z gradients become less severe. This lengthening is increased as σ becomes smaller so the $\sigma = 0.5$ vortices at the bottom of Figure 5.1 rotate even slower than $\sigma = 2$ vortices. Also recall that θ_z^0 is equal to the leading-order vorticity $u_y^0 - v_x^0$, so a smaller θ_z^0 gradient means slower rotation.

5.1.2 Vortex census statistics

The ensemble (using $\nu = 10^{-9}$) included 34 runs to $t = 500$ with $\sigma = 4$ and $\sigma \to \infty$. Also, a mini-ensemble (using $\nu = 10^{-8}$) was run, which included 7 runs each with $\sigma = 10$ and $\sigma = 4$, and 17 runs with $\sigma = 1$. Simulation time per run was approximately 10 hours using 4 parallel 833 MHz processors on a DEC Alpha Cluster. The majority of that time was spent in the potential vorticity inversion subroutine which calls 16 256×256 Discrete Fourier Transforms. Examples of typical freely-decaying turbulence simulations for various σ values are shown in Figure 5.3. Typical initial conditions are shown in Figure 5.3(a), but note that RMS(S) in the initial conditions of each of the three runs is different (see the end of Section 4.4 for details on normalization). Figure 5.3(d) was run with $\sigma = 1$ and diffusion

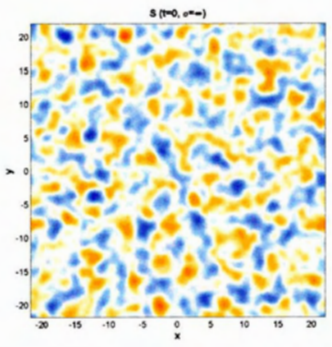

(a) Initial S

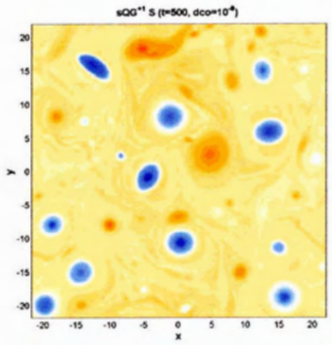

(b) sQG^{+1} ($t = 500$, $\nu = 10^{-9}$)

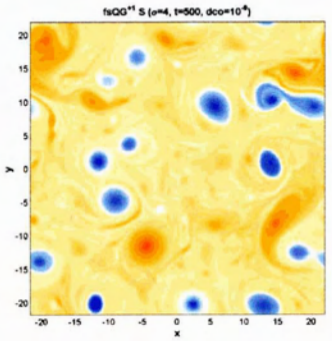

(c) fsQG^{+1} ($\sigma = 4$, $t = 500$, $\nu = 10^{-9}$)

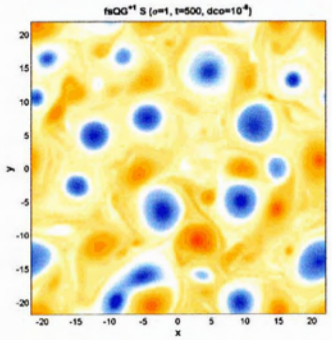

(d) fsQG^{+1} ($\sigma = 1$, $t = 500$, $\nu = 10^{-8}$)

Figure 5.3: Plots of S in freely-decaying turbulence runs. (a) Initially random S. (b) At $t = 500$, the sQG^{+1} system evolves into coherent structures with surface warming. Cyclones are more intense than anticyclones and do not tend to axisymmetrize. (c) The asymmetry in the fsQG^{+1} solution with $\sigma = 4$ is similar to (b), while (d) the $\sigma = 1$ solution (with more diffusion) shows more diffuse cyclones and more significant anticyclones.

constant $\nu = 10^{-8}$ while the other two simulations used $\nu = 10^{-9}$.

The census statistics for both ensembles are shown in Tables 5.1 (mean data) and 5.2 (standard deviations). Note that the amplitudes of S first have the mean subtracted ($S - \bar{S}$), then are re-normalized using the equation

$$S \to \frac{S}{1 + 0.82/\sigma} \tag{5.1}$$

from Section 4.4. From the mean data, increasing ν from 10^{-9} to 10^{-8} has a slight sym-

Table 5.1: Census MEAN vortex radius, amplitude and number of vortices ($\sigma \to \infty$ represents sQG^{+1}). All ratios are cyclone/anticyclone. Data for $\nu = 10^{-8}$: 17 runs at $\sigma = 1$, 7 runs at $\sigma = 4$ and $\sigma = 10$, for $\nu = 10^{-9}$: 34 runs each.

Measure	Vortex	$\nu = 10^{-8}$			$\nu = 10^{-9}$	
		$\sigma = 1$	$\sigma = 4$	$\sigma = 10$	$\sigma = 4$	$\sigma \to \infty$
radius	cyclone	6.57	5.83	5.72	5.41	4.85
	anticyclone	6.07	5.33	4.92	4.69	4.32
	ratio	1.08	1.09	1.16	1.15	1.12
amplitude	cyclone	3.00	3.09	3.05	3.35	3.55
	anticyclone	1.67	1.67	1.58	1.46	1.51
	ratio	1.80	1.85	1.93	2.29	2.35
number of vortices	cyclone	14.65	11.86	10.00	12.54	10.35
	anticyclone	16.71	15.43	15.57	19.08	15.62
	ratio	0.88	0.77	0.64	0.66	0.66

metrizing effect. With $\nu = 10^{-8}$, cyclones are slightly weaker in amplitude and anticyclones are slightly larger in amplitude than for $\nu = 10^{-9}$. Also, the mean radii for both cyclones and anticyclones are increased with $\nu = 10^{-8}$. The $\nu = 10^{-9}$ and $\sigma = 4$ ensemble exhibits slightly less asymmetry in terms of the ratio of the mean amplitude between cyclones and anticyclones than the $\sigma \to \infty$ ensemble. The most notable symmetrization though is in the $\nu = 10^{-8}$ ensemble where amplitude, radii, and number of vortices tend to symmetrize as σ gets smaller. The important information in the standard deviation data (Table 5.2) is that for both $\nu = 10^{-9}$ and $\nu = 10^{-8}$, the ratio of cyclone to anticyclone radii standard deviations increases as σ becomes smaller[1]. This means that the tendency found by Hakim et al. in [8] for cyclones to prefer a distinct length scale (anticyclones did not) is weakened as σ becomes smaller.

[1]The radius ratio in the $\sigma = 1$ column is only 0.81 because 17 runs with $\sigma = 1$ were made instead of 7 as with $\sigma = 4$ and $\sigma = 10$ so the standard deviations for the $\sigma = 1$ data contain different sample size error.

Table 5.2: Census STANDARD DEVIATION of vortex radius, amplitude and number of vortices ($\sigma \to \infty$ represents sQG^{+1}). All ratios are cyclone/anticyclone. Data for $\nu = 10^{-8}$: 17 runs at $\sigma = 1$, 7 runs at $\sigma = 4$ and $\sigma = 10$, for $\nu = 10^{-9}$: 34 runs each.

Measure	Vortex	$\nu = 10^{-8}$			$\nu = 10^{-9}$	
		$\sigma = 1$	$\sigma = 4$	$\sigma = 10$	$\sigma = 4$	$\sigma \to \infty$
radius	cyclone	1.64	1.63	1.60	1.49	1.26
	anticyclone	2.03	1.93	2.04	2.03	1.87
	ratio	0.81	0.84	0.78	0.73	0.67
amplitude	cyclone	0.81	0.90	1.16	0.98	0.91
	anticyclone	0.75	0.79	0.75	0.81	0.87
	ratio	1.08	1.14	1.55	1.21	1.05
number of vortices	cyclone	1.90	1.35	1.41	1.71	1.81
	anticyclone	3.06	2.99	2.23	3.72	2.92
	ratio	0.62	0.45	0.63	0.46	0.62

5.2 Cyclone-anticyclone asymmetry

Plots of single vortices in Section 5.1.1 showed that cyclones do not tend to axisymmetrize as much as single anticyclones, even for $\sigma < 1$. On the other hand, mean and standard deviation data from Section 5.1.2 indicated symmetry trends as σ becomes small. The census data is plotted in amplitude and radius (mean) histograms, as well as radius versus amplitude joint probability distributions in Figures 5.4 and 5.5. In the histograms the vertical gray lines indicate one standard deviation, and in the probability distributions the contours are interpolated constant-density contours (.01,.02,.03, etc.). The plots indicate a slight weakening in the asymmetry at $\sigma = 4$, and Figures 5.5(b) and 5.5(f) show near cyclone-anticyclone symmetry for $\sigma = 1$ and $\nu = 10^{-8}$. No simulations were attempted with even smaller σ (as in Figure 3.4) for stability reasons because of how S was normalized by RMS leading-order wind. Simulations with $\sigma = 1$ and $\nu = 10^{-9}$ were attempted but only for a few initial conditions did the simulation maintain stability.

5.3 Surface warming

Mean surface warming ($\bar{\theta}^s > 0$) is an effect observed in sQG^{+1} that is believed to be caused by warm (cold) air rising (sinking) [2]. Part of the goal of this study is determine the effect

[2] Actually in [8] mean surface cooling was observed because the surface in that study was below the domain (on the ground).

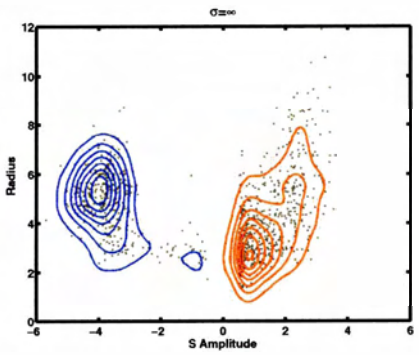

(a) $\sigma \to \infty$: radius vs. amplitude

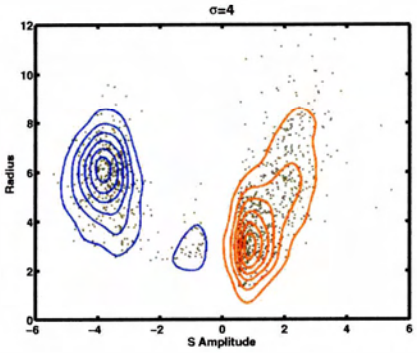

(b) $\sigma = 4$: radius vs. amplitude

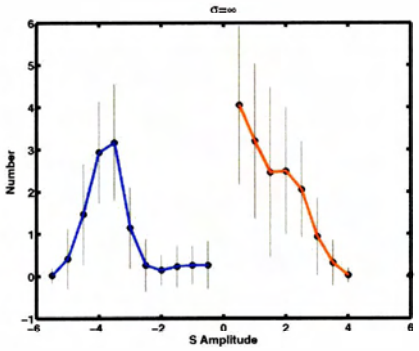

(c) $\sigma \to \infty$: amplitude

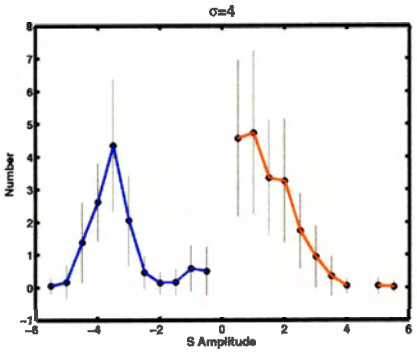

(d) $\sigma = 4$: amplitude

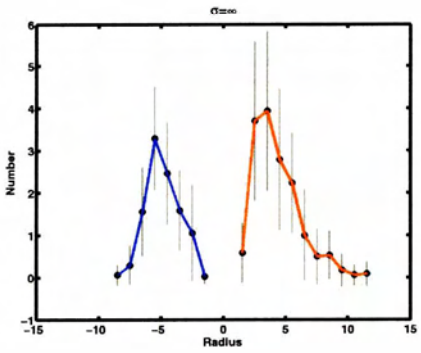

(e) $\sigma \to \infty$: radius

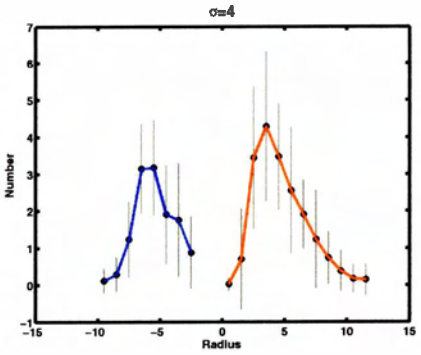

(f) $\sigma = 4$: radius

Figure 5.4: Vortex census data at $t = 500$ with $\nu = 10^{-9}$ for sQG^{+1} $\sigma \to \infty$ (left) and fsQG^{+1} $\sigma = 4$ (right) showing (a), (b) vortex radius as a function of $S - \bar{S}$, (c), (d) ensemble-mean vortex amplitude, and (e), (f) radius. The census data is from 34 runs with $\sigma \to \infty$ and 34 runs with $\sigma = 4$. In each plot, cyclones are on the left, anticyclones on the right.

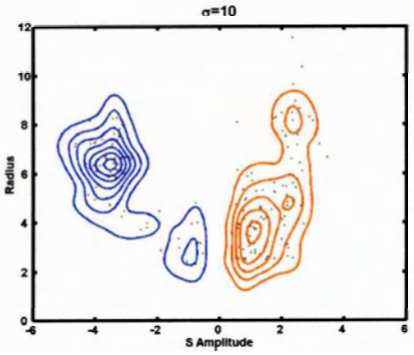

(a) $\sigma = 10$: radius vs. amplitude

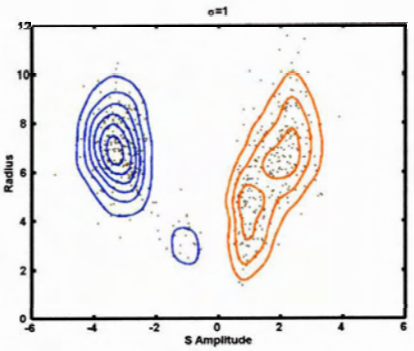

(b) $\sigma = 1$: radius vs. amplitude

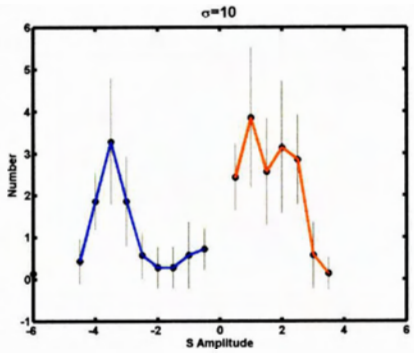

(c) $\sigma = 10$: amplitude

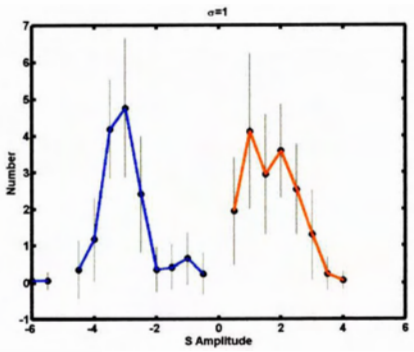

(d) $\sigma = 1$: amplitude

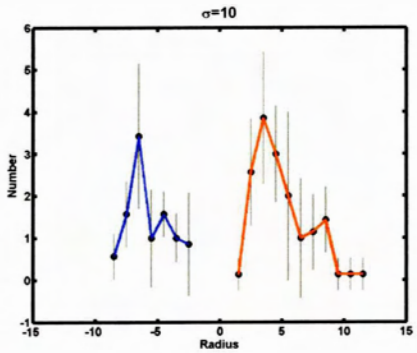

(e) $\sigma = 10$: radius

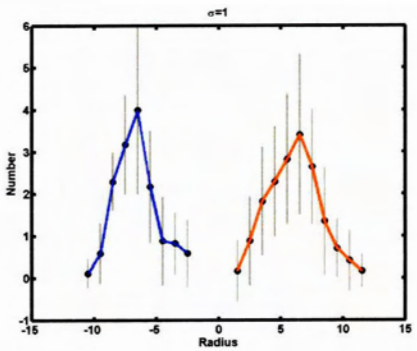

(f) $\sigma = 1$: radius

Figure 5.5: Vortex census data at $t = 500$ with $\nu = 10^{-8}$ for fsQG^{+1} $\sigma = 10$ (left) and $\sigma = 1$ (right) showing (a), (b) vortex radius as a function of $S - \bar{S}$, (c), (d) ensemble-mean vortex amplitude, and (e), (f) radius. The census data from 7 runs with $\sigma = 10$ and 17 runs with $\sigma = 1$. In each plot, cyclones are on the left, anticyclones on the right.

of finite σ on mean surface warming. As Figure 5.6 shows, the effect of decreasing σ from 4 to 1 has little effect on the mean h and θ^s; apparently the surface height drifts upwards regardless of the stiffness (except if $\sigma \to \infty$ of course), possibly because there is no pressure from above the surface. The mean plots appear as though the surface is actually exhibiting mean cooling because $\bar{\theta}^s$ decreases with time. But recall that θ^s is only the disturbance potential temperature and S is the total potential temperature on the surface ($S \equiv \theta^T|^s$) and $\bar{S}$ is increasing with time. The variance in surface height is quite sensitive to its stiffness even though the mean is not. Notice that the variance of θ^s is approximately the same for both $\sigma = 4$ and $\sigma = 1$ (because both are normalized by leading-order RMS winds, see the end of Section 4.4 for reasoning), but the variance of height h decreases significantly for $\sigma = 4$. A flexible surface certainly absorbs some of the energy in a given S field, so clearly for the same S, the variance in θ^s would be less for a flexible surface than a rigid surface. This assertion agrees with the observation in Section 5.1.1 that small σ vortices rotate slower than large σ vortices because the variance of h absorbs part of the the variance of θ, which is equal to the RMS leading-order winds.

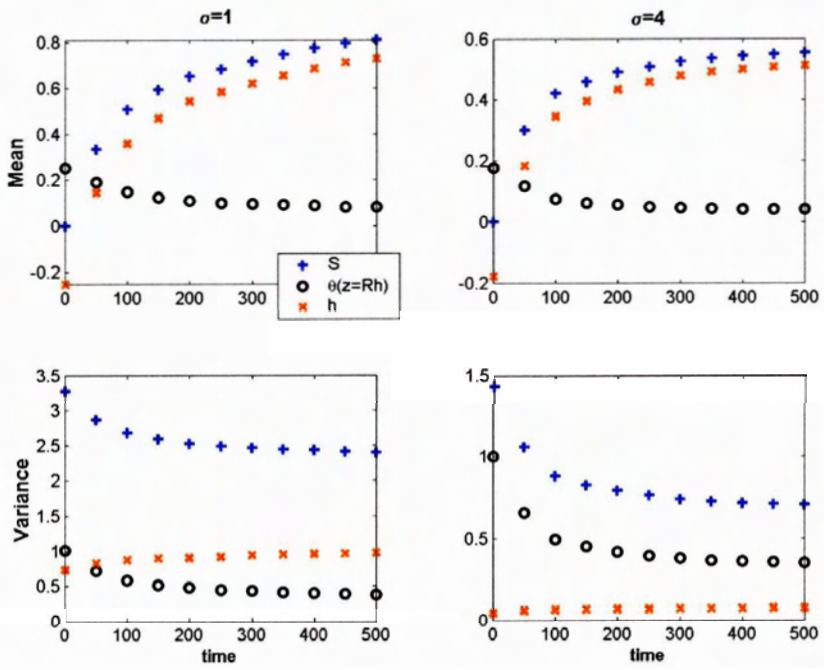

Figure 5.6: Plot of mean and variance of S, h, and θ^s versus time for $\sigma = 1$ and $\sigma = 4$ with the same initial conditions and $\nu = 10^{-8}$. All plots are normalized with leading-order RMS winds so RMS S is different for the left and right plots, which is why the axes are scaled differently.

Chapter 6

Summary and conclusions

This work attempts to reconcile the seemingly contradictory results between a study of cyclone-anticyclone asymmetry in the shallow-water regime [14] and a next-order corrected quasigeostrophic study [8]. This work also serves as the next step in the sQG^{+1} research plan illustrated in Figure 1.1.

The first two chapters introduce rotating, stratified fluid dynamics and the problem of asymmetric vortex organization on the tropopause. Chapter 1 gives a brief summary of some of the literature available on the subject. Chapter 2 introduces the primitive equations of atmospheric motion and outlines quasigeostrophic theory, including next-order corrections. The shallow-water equations are also listed for completeness.

Chapter 3 introduces the theory of the next step in surface quasigeostrophy, allowing the previously fixed surface to become flexible. The inclusion of the stratification constant (σ) in (3.1) parameterizes the surface rigidity and transforms the sQG^{+1} equations into free-surface fsQG^{+1} equations. The importance of the boundary conditions cannot be overstated, they are vital to the behavior of the entire fsQG^{+1} system. In fsQG^{+1}, the conserved quantity S is equal to the total potential temperature at the surface (as in sQG^{+1}) except now the surface is at a nonzero height $z = Rh(x, y, t)$. The result is that S becomes a Robin boundary condition in the Laplace problem for Φ^0 in (3.10). The next-order potentials Φ^1, F^1, and G^1 are computed from Φ^0 and the next-order boundary conditions (3.8) and (3.11). Chapter 3 ends with plots of axisymmetric (Gaussian) cyclone and anticyclonic disturbances for small and large σ values. For $\sigma = 0.25$, next-order corrections positively affect the disturbance height (h) for both cyclones and anticyclones, making a given perturbation S more intense when anticyclonic (like shallow-water). On the other hand with $\sigma = 4$

(which is closer to sQG^{+1}) a given disturbance in S is negatively affected by the next-order corrections, making cyclones more intense than anticyclones. The quadratic nature of the boundary value for the harmonic part of Φ^1 (in (B.9) of Appendix B) indicates that the sign of the next-order correction is dependent on σ and not the sign of Φ^0. However, the physical interpretation of the boundary value is not understood.

Chapter 4 describes some of the salient implementation details, most of which are familiar from sQG^1, except for the last part on scaling. The robin boundary condition on the surface of fsQG^{+1} presents a scaling problem because the root mean square of the leading order winds (u^0 and v^0) does not normalize S when σ is finite. Leading-order winds only normalize the Φ_z^0 part of $S = \frac{1}{\sigma}\Phi^0 + \Phi_z^0$, which means the $\frac{1}{\sigma}\Phi^0$ term grows as σ becomes small. The next-order potentials also grow, increasing the effects of nonlinearity and destabilizing the decaying turbulence simulations. Runs with $\sigma = 4$ and hyperdiffusion constant $\nu = 10^{-9}$ were rarely affected by nonlinear instabilities, however $\sigma = 1$ and $\nu = 10^{-9}$ runs often became unstable. Instead of increasing the hyperdiffusion (to $\nu = 10^{-8}$ as done in the mini-ensemble), a better approach is likely to decrease the Rossby number R (from 0.1 to 0.05) which controls the amount on nonlinearity in the primitive equations (2.10).

The main results of the study are presented in Chapter 5. Given the same leading-order winds, vortices in fsQG^{+1} (with finite σ) rotate slower than sQG^{+1} vortices because the free-surface allows for height changes that decrease θ_z which corresponds to $u_y - v_x$ (horizontal vorticity) at leading-order. The vortex census data exhibits a weakening in the asymmetry between cyclones and anticyclones as σ becomes smaller. Table 5.1 shows that the ratio of mean amplitudes between cyclones and anticyclones tends towards unity as σ becomes smaller for both $\nu = 10^{-9}$ and $\nu = 10^{-8}$. Table 5.2 shows the ratio of standard deviations between cyclones and anticyclones tends towards as σ becomes smaller, meaning that the tendency for cyclones to prefer a distinct length scale (from sQG^{+1}) is weakened in fsQG^{+1}. However, the tendencies listed above are modest, for example from $\sigma = \infty$ to $\sigma = 4$ (with $\nu = 10^{-9}$) the ratio of cyclone to anticyclone mean amplitudes only decreases from 2.35 to 2.29. For a more illuminating test of weakened vortex asymmetry, it seems that $\sigma \leq 1$ with $\nu = 10^{-9}$ is necessary. Chapter 5 also addresses the issue of mean surface warming, which is an indicator of vortex asymmetry because under mean warming cyclones of equal magnitude to anticyclones deviate more from the mean. The hypothesis in [8] is that top surface warming is due to warm air rising and cold air sinking. In fsQG^{+1}, finite σ leads to a different effect, as increases in the mean of $S = h + \theta^s$ are absorbed by the mean of h

and not $\bar{\theta}^s$ (see Figure 5.6). The physical reason for the mean of h to absorb the mean of S is not understood. On the other hand, the variance of S, h, and θ^s behave as expected, smaller σ implies larger variance in h relative to θ^s, which just means that the surface is indeed more flexible.

The purpose of this thesis work was to advance the sQG^{+1} model developed in [8] one step closer to a true tropopause model. Specifically, we asked what effect a free-surface would have on sQG^{+1}? would cyclone-anticyclone asymmetry in $fsQG^{+1}$ depend on the value of the surface rigidity σ? we found vortex asymmetry to be weakened as we expected, but many of the details of the $fsQG^{+1}$ dynamics are not yet understood. The time-independent axisymmetric solution showed near cyclone-anticyclone symmetry (in the height field h) by $\sigma = 1$ and reversal of the asymmetry at $\sigma = 0.25$, while the decaying turbulence vortex census showed only modest weakening of the asymmetry at $\sigma = 1$. Why does a single axisymmetric vortex behave so much differently than a set of freely-evolving cyclones and anticyclones? Perhaps the structure of cyclones favors them over equally strong anticyclones. In certain $fsQG^{+1}$ turbulence simulations, strong oval shaped cyclones behaved like propellers, dispersing the outer regions of the more axisymmetric anticyclones. So perhaps the predominance of cyclones in freely-decaying turbulence has as much to do with preferred shape of cyclones (in Figure 5.1) as with the sign of the next-order corrections.

Another question is what causes the asymmetry of single vortices to reverse as the surface becomes more flexible? Polvani [14] argued that anticyclones are stronger than cyclones in shallow-water theory because as anticyclones raise the surface they increase the "radius of deformation". The radius of deformation defines the length scale of the problem and decreases the Rossby number, making rotation stronger for anticyclones than cyclones. Perhaps we have observed this effect for single axisymmetric vortices, but the above "propeller effect" combined with continuous stratification (warm air rising, cold air sinking) dominate the formation of coherent structures in turbulence simulations. Further unresolved questions include the mean behavior of S over time in the turbulence simulations. The dependence on σ of the mean of S over time is unknown because we normalized the initial conditions by root mean square winds. Also, the reason why h absorbed nearly all of the mean of S is not known.

The developmental stage of the $fsQG^{+1}$ is now complete. A larger vortex sample will help characterize the dynamics of the model, but the most important future work is to understand the physical consequences of the free-surface. In the sQG^{+1} model frontogenesis, which is the

formation or intensification of fronts between regions of different temperature, was identified as a likely source of vortex asymmetry. As small scales in potential temperature develop on the surface, warm regions tend to expand and cold regions contract. Also, in sQG^{+1} anticyclones tended to merge producing larger scales, while cyclones tended not to merge. The goal for future $fsQG^{+1}$ work will be to understand how a free-surface affects these convergence and divergence effects.

Appendix A

Details of next-order fsQG^{+1} inversion

At order Rossby number the surface boundary conditions from (3.7) and (3.2) are

$$h^1 + \Phi^1_z + G^1_x - F^1_y + h^0\Phi^0_{zz} = 0 \tag{A.1}$$

$$\frac{1}{2}(h^0)^2 - \sigma h^1 + \phi^1 + h^0\Phi^0_z = 0, \tag{A.2}$$

which contain 5 unknowns (h^1,Φ^1,G^1,F^1,ϕ^1) because $\phi^0 = \Phi^0$ and $h^0 = \Phi^0/\sigma$. But ϕ^1 can be eliminated using the fact that $\phi^1_z = \theta^1$:

$$\begin{aligned}
\phi^1_z = \theta^1 &= \Phi^1_z + G^1_x - F^1_y \\
\Rightarrow \phi^1_z &= \left(\Phi^0_z\Phi^0_z - \frac{1}{2}\Phi^0_x\Phi^0_x - \frac{1}{2}\Phi^0_y\Phi^0_y\right)_z + \tilde{\Phi}^1_z + \tilde{G}^1_x - \tilde{F}^1_y \\
\Rightarrow \phi^1 &= \left(\Phi^0_z\Phi^0_z - \frac{1}{2}\Phi^0_x\Phi^0_x - \frac{1}{2}\Phi^0_y\Phi^0_y\right) + \tilde{\Phi}^1 + \int_{-\infty}^{0} \tilde{G}^1_x - \tilde{F}^1_y \, dz
\end{aligned} \tag{A.3}$$

The harmonic ambiguity of Equation (2.15) allows one degree of freedom, and choosing

$$\tilde{G}^1_x - \tilde{F}^1_y = 0 \tag{A.4}$$

on the surface makes a convenient boundary condition. Equation (A.4) also implies that ϕ^1 is a function of $\tilde{\Phi}^1$ and Φ^0 only because both $\tilde{F}^1$ and $\tilde{G}^1$ are harmonic so $\tilde{G}^1_x - \tilde{F}^1_y = 0$ everywhere in the domain in Equation (A.3). Thus, inserting (A.3) into (A.2) and

combining with (A.1) to eliminate h^1 gives a Laplace problem for $\tilde{\Phi}^1$:

$$\begin{cases} \nabla^2\tilde{\Phi}^1 = 0 \\ \frac{1}{\sigma}\tilde{\Phi}^1(z=0) + \tilde{\Phi}^1_z(z=0) = f(\Phi^0, \Phi^0_z, \Phi^0_{zz}) \\ \text{decay}(z \to -\infty), \text{ periodicity in } (x,y) \end{cases} \tag{A.5}$$

where

$$\begin{aligned} f(\Phi^0, \Phi^0_z, \Phi^0_{zz}) = &- \left(\Phi^0_z\Phi^0_z - \frac{1}{2}\Phi^0_x\Phi^0_x - \frac{1}{2}\Phi^0_y\Phi^0_y\right)_z - \frac{1}{\sigma}\Phi^0\Phi^0_{zz} - \frac{1}{2\sigma^3}(\Phi^0)^2 \\ &- \frac{1}{\sigma}\left(\Phi^0_z\Phi^0_z - \frac{1}{2}\Phi^0_x\Phi^0_x - \frac{1}{2}\Phi^0_y\Phi^0_y\right) - \frac{1}{\sigma^2}\Phi^0\Phi^0_z, \end{aligned}$$

evaluated at the surface. So $\tilde{\Phi}^1$ is given by

$$\tilde{\Phi}^1(x,y,z,t) = \frac{1}{4\pi^2}\iint_{-\infty}^{\infty} \frac{1}{m+\frac{1}{\sigma}}\hat{f}e^{i(kx+ly)}e^{mz}\,dkdl, \tag{A.6}$$

where $m = \sqrt{k^2+l^2}$.

Finding w^0 at the surface is possible if Equation (3.3), the kinematic free surface boundary condition, is combined with the θ primitive equation (2.10). In (3.3) the advective part is zero at leading-order because at leading-order

$$-u^s h_x - v^s h_y \Rightarrow \Phi^0_y h^0_x - \Phi^0_x h^0_y = J\left(\frac{1}{\sigma}\Phi^0, \Phi^0\right) = 0. \tag{A.7}$$

Therefore (3.3) and the leading-order primitive equation for θ give

$$\begin{aligned} w^0 &= -\theta^0_t - u^0\theta^0_x - v^0\theta^0_y = \frac{1}{\sigma}\Phi^0_t \\ &\Rightarrow \left(\frac{1}{\sigma}\Phi^0 + \Phi^0_z\right)_t = J(\Phi^0_z, \Phi^0), \end{aligned} \tag{A.8}$$

since $\theta^0 = \Phi^0_z$. This is similar to the familiar Robin condition of Equation (3.10), but now operating on Φ^0_t. The z and t derivatives commute since the condition holds for all time, including $t = 0$, so w^0 is

$$w^0(x,y,z,t) = \frac{1}{4\sigma\pi^2}\iint_{-\infty}^{\infty} \frac{1}{m+\frac{1}{\sigma}}\widehat{J(\Phi^0_z, \Phi^0)}e^{i(kx+ly)}e^{mz}\,dkdl. \tag{A.9}$$

To solve for $\tilde{G}^1_z$ and $\tilde{F}^1_z$, we need another boundary condition in addition to the harmonic ambiguity, Equation (A.4). This condition comes from Equations (2.18) and (3.3),

$$F^1_x + G^1_y = w^0 = h^0_t + J(\Phi^0, h^0). \tag{A.10}$$

where $J(\Phi^0, h^0)$ is identically zero because in (3.9) Φ^0 is proportional to h^0. Solving for $\tilde{G}_z^1$ and $\tilde{F}_z^1$ proceeds as follows

$$\begin{aligned} \tilde{F}_x^1 + \tilde{G}_y^1 &= w^0 + (\Phi_x^0 \Phi_z^0)_y - (\Phi_y^0 \Phi_z^0)_x \\ &= w^0 + J(\Phi^0, \Phi_z^0) \\ \Rightarrow \widehat{\tilde{F}_x^1} + \widehat{\tilde{G}_y^1} &= \frac{m}{m + \frac{1}{\sigma}} \widehat{J(\Phi^0, \Phi_z^0)}. \end{aligned} \tag{A.11}$$

Combining (A.4) with (A.11) in Fourier space gives

$$\begin{aligned} \widehat{\tilde{F}_z^1} &= \frac{-ik}{m + \frac{1}{\sigma}} \widehat{J(\Phi^0, \Phi_z^0)} \\ \widehat{\tilde{G}_z^1} &= \frac{-il}{m + \frac{1}{\sigma}} \widehat{J(\Phi^0, \Phi_z^0)} \end{aligned} \tag{A.12}$$

where multiplication by ik, il, or m constitute x, y, or z differentiation in the Fourier domain. Thus, $\tilde{F}_z^1$ and $\tilde{G}_z^1$ are

$$\begin{aligned} \tilde{F}_z^1(x,y,z,t) &= \frac{1}{4\pi^2} \iint_{-\infty}^{\infty} \frac{-ik}{m + \frac{1}{\sigma}} \widehat{J(\Phi^0, \Phi_z^0)} e^{i(kx+ly)} e^{mz} \, dkdl, \\ \tilde{G}_z^1(x,y,z,t) &= \frac{1}{4\pi^2} \iint_{-\infty}^{\infty} \frac{-il}{m + \frac{1}{\sigma}} \widehat{J(\Phi^0, \Phi_z^0)} e^{i(kx+ly)} e^{mz} \, dkdl. \end{aligned} \tag{A.13}$$

Appendix B

Details of next-order axisymmetric fsQG^{+1} inversion

Solving for the next-order correction Φ^1 is simplified by noticing that $\tilde{F}^1$ and $\tilde{G}^1$ are zero in the axisymmetric case. Since S is axisymmetric, then Φ^0 is also axisymmetric because in (4.1) Φ^0 is a linear function of S with no azimuthal dependence. By the same argument, Φ^0_z is also axi-symmetric. In this case, Equation (A.9) says that $w^0 = 0$ because the Jacobian in polar coordinates is defined as

$$J(f,g) \equiv f_x g_y - g_x f_y = \frac{1}{r} f_r g_\alpha - f_\alpha g_r. \tag{B.1}$$

where α is the azimuthal coordinate. We also know from Equation (A.11) that if S is axisymmetric

$$\tilde{F}^1_x + \tilde{G}^1_y = w^0 + J(\Phi^0, \Phi^0_z) = 0. \tag{B.2}$$

This result combined with the boundary condition (harmonic ambiguity) in (A.4) means $\tilde{F}^1$ and $\tilde{G}^1$ can be set to zero since

$$\left.\begin{array}{l} \tilde{F}^1_x + \tilde{G}^1_y = 0 \\ \tilde{G}^1_x - \tilde{F}^1_y = 0 \end{array}\right\} \quad \Rightarrow \quad \tilde{F}^1 \text{ and } \tilde{G}^1 \text{ are arbitrary constants.} \tag{B.3}$$

Advection of S (3.13) now becomes $S_t = 0$ because

$$\begin{aligned} S_t &= -u^s S_x - v^s S_y \\ &= \Phi_y S_x - \Phi_x S_y + F_z S_x + G_z S_y \\ &= (\Phi_z^0 \Phi_y^0)_z S_x - (\Phi_z^0 \Phi_x^0)_z S_y \\ &= J(S, \Phi^0)\Phi_{zz}^0 + J(S, \Phi_z^0)\Phi_z^0 = 0, \end{aligned} \tag{B.4}$$

since S, Φ^0 and Φ_z^0 are axisymmetric and have no dependence in the azimuthal direction (see the definition of the Jacobian in (Eq:defjac)). so the axisymmetric problem is time independent.

Solving for a Robin condition on $\tilde{\Phi}^1$ is now possible using Equations (A.1) and (A.2) which become

$$0 = h^1 + \tilde{\Phi}_z^1 + \left(\Phi_z^0 \Phi_z^0 - \frac{1}{2}\Phi_x^0 \Phi_x^0 - \frac{1}{2}\Phi_y^0 \Phi_y^0 \right)_z + h^0 \Phi_{zz}^0, \tag{B.5}$$

$$0 = -\sigma h^1 + \tilde{\Phi}^1 + \left(\Phi_z^0 \Phi_z^0 - \frac{1}{2}\Phi_x^0 \Phi_x^0 - \frac{1}{2}\Phi_y^0 \Phi_y^0 \right) + \frac{1}{2}(h^0)^2 + h^0 \Phi_z^0, \tag{B.6}$$

and noting that

$$\Phi_x^0 \Phi_x^0 + \Phi_y^0 \Phi_y^0 = (\Phi_r^0)^2 + \frac{1}{r^2}(\Phi_\theta^0)^2 = (\Phi_r^0)^2. \tag{B.7}$$

in polar coordinates. Equations (B.5) and (B.6) together can eliminate h^1 and form a Robin condition on $\tilde{\Phi}^1$. Thus the solution to the Laplace problem in (2.22) for $\tilde{\Phi}^1$ (with decay as $z \to -\infty$) is given by

$$\tilde{\Phi}^1(r, z) = \int_0^\infty \frac{m}{m + 1/\sigma} \hat{f}(m) J_0(mr) e^{mz}\, dm \tag{B.8}$$

where $\hat{f}(m)$ comes from the Robin condition at the surface

$$\begin{aligned} \hat{f}(m) &= \int_0^\infty f(r, z = 0) J_0(mr) r\, dr \\ f(r, z = 0) &= -2\Phi_z^0 \Phi_{zz}^0 + \Phi_r^0 \Phi_{rz}^0 - \frac{1}{\sigma}\Phi^0 \Phi_{zz}^0 - \frac{1}{\sigma}(\Phi_z^0)^2 + \frac{1}{2\sigma}(\Phi_r^0)^2 \\ &\quad - \frac{1}{2\sigma^3}(\Phi^0)^2 - \frac{1}{\sigma^2}\Phi^0 \Phi_z^0. \end{aligned} \tag{B.9}$$

Next-order velocities and potential temperature are needed to compare the 2D, time

dependent Fourier solutions with the axisymmetric Hankel solution. The next-order axisymmetric wind speed (V) in the azimuthal (α) direction is computed using polar coordinates

$$\begin{aligned} V &= \begin{pmatrix} u \\ v \end{pmatrix} \cdot \begin{pmatrix} -\sin(\alpha) \\ \cos(\alpha) \end{pmatrix} \\ &= (\Phi_y + F_z)\sin(\alpha) + (\Phi_x - G_z)\cos(\alpha) \\ &= (\Phi_x \cos(\alpha) + \Phi_y \sin(\alpha)) + F_z \sin(\alpha) - G_z \cos(\alpha) \\ &= \Phi_r + R(\Phi_z^0(\Phi_y^0 \sin(\alpha) + \Phi_x^0 \cos(\alpha)) + \tilde{F}^1 \sin(\alpha) - \tilde{G}^1 \cos(\alpha))_z \\ &= \Phi_r^0 + R(\tilde{\Phi}_r^1 + 2\Phi_z^0 \Phi_{zr}^0 + \Phi_{zz}^0 \Phi_r^0). \end{aligned} \tag{B.10}$$

The next-order potential temperature (θ) is computed similarly

$$\begin{aligned} \theta &= \Phi_z^0 + R(\Phi_z^1 + G_x^1 - F_y^1) \\ &= \Phi_z^0 + R(\tilde{\Phi}_z^1 + \Phi_z^0 \Phi_{zz}^0 - (\Phi_x^0 \Phi_z^0)_x - (\Phi_y^0 \Phi_z^0)_y) \\ &= \Phi_z^0 + R(\tilde{\Phi}_z^1 + (\Phi_z^0 \Phi_z^0 - \frac{1}{2}(\Phi_x^0 \Phi_x^0 + \Phi_y^0 \Phi_y^0))_z) \\ &= \Phi_z^0 + R(\tilde{\Phi}_z^1 + 2\Phi_z^0 \Phi_{zz}^0 - \Phi_r^0 \Phi_{zr}^0). \end{aligned} \tag{B.11}$$

Bibliography

[1] Acheson, D.J., 1990: *Elementary Fluid Dynamics.* Oxford University Press, Inc., 397 pp.

[2] Blumen, W., 1978: Uniform Potential Vorticity Flow: Part I. Theory of Wave Interaction and Two-Dimensional Turbulence. *Journal of the Atmospheric Sciences*, **35**, 774-783.

[3] Charney, J.G., 1948: On the scale of atmospheric motions. *Geofysiske Publikasjoner*, **17** (2), 1-17.

[4] Cushman-Roisin, B. and B. Tang, 1990: Geostrophic Turbulence and Emergence of Eddies beyond the Radius of Deformation. *Journal of Physical Oceanography*, **20**, 97-113.

[5] Cushman-Roisin, B., 1994: *Introduction to Geophysical Fluid Dynamics.* Prentice-Hall, Inc., 320 pp.

[6] Dunlop, S., 2001: *Dictionary of Weather.* Oxford University Press, 269 pp.

[7] Durran, D.R., 1998: *Numerical Methods for Wave Equations in Geophysical Fluid Dynamics.* Springer-Verlag, Inc., 465 pp.

[8] Hakim, G.J., C. Snyder, D.J. Muraki, 2002: A New Surface Model for Cyclone-Anticyclone Asymmetry. *Journal of the Atmospheric Sciences*, **59**, 2405-2420.

[9] Held, I.M., R.T. Pierrehumbert, S.T. Garner, K.L. Swanson, 1995: Surface quasi-geostrophic dynamics. *Journal of Fluid Mechanics*, **282**, 1-20.

[10] Juckes, M., 1994: Quasigeostrophic Dynamics of the Tropopause. *Journal of the Atmospheric Sciences*, **51**, 2756-2768.

[11] Mellor, G.L., 1996: *Inroduction to Physical Oceanography.* AIP Press, 260 pp.

[12] Muraki, D.J., and G. Hakim, 2001: Balanced Asymmetries of Waves on the Tropopause. *Journal of the Atmospheric Sciences*, **58**, 237-252.

[13] Muraki, D.J., C. Snyder, and R. Rotunno, 1999: The Next-Order Corrections to Quasi-geostrophic Theory. *Journal of the Atmospheric Sciences*, **56**, 1547-1560.

[14] Polvani, L.M., J.C. McWilliams, M.A. Spall, and R. Ford, 1994: The coherent structures of shallow-water turbulence: Deformation-radius effects, cyclone/anticyclone asymmetry and gracity-wave generation. *CHAOS*, **4**, 177-186.

[15] Randall, D.A., 2003: *The Shallow Water Equations.* Course notes, available at http://kiwi.atmos.colostate.edu/group/dave/drweb/Shallow_water.pdf.

[16] Sanders, F., 1988: Life history of mobile troughs in the upper westerlies. *Monthly Weather Review*, **116**, 2629-2648.

[17] Sneddon, I.N., 1951: *Fourier Transforms.* McGraw-Hill Book Company, Inc., 542 pp.

[18] Thorpe, A.J., 1986: Synoptic Scale Disturbances with Circular Symmetry. *Monthly Weather Review*, **114**, 1384-1389.

[19] Trefethen, L.N., 1996: *Finite Difference and Spectral Methods for Ordinary and Partial Differential Equations.* Unpublished text, available at http://web.comlab.ox.ac.uk/oucl/work/nick.trefethen/pdetext.html.

[20] Wirth, V., 2001: Cyclone-Anticyclone Asymmetry Concerning the Height of the Thermal and the Dynamical Tropopause. *Journal of the Atmospheric Sciences*, **58**, 26-37.

[21] Yavneh, I., A.F. Shehepetkin, J.C. McWilliams, and L.P. Graves, 1997: Multigrid Solution of Rotating, Stably Stratified Flows: The Balance Equations and Their Turbulent Dynamics. *Journal of Computational Physics*, **136**, 245-262.